PHYSICAL REVIEW MATERIALS **6**, 025404 (2022)

Defect formation in Yb-doped $CsPbCl_3$ from first principles with implications for quantum cutting

David E. Sommer
Department of Physics, University of Washington, Seattle, Washington 98195, USA

Daniel R. Gamelin
Department of Chemistry, University of Washington, Seattle, Washington 98195, USA

Scott T. Dunham
Department of Electrical Engineering, University of Washington, Seattle, Washington 98195, USA

(Received 11 August 2021; accepted 27 January 2022; published 22 February 2022)

Exceptionally high experimental photoluminescence quantum yields attributed to highly efficient quantum cutting have recently been observed in ytterbium-doped inorganic metal-halide perovskites such as Yb:CsPb(X = Cl, Br)$_3$. Combined with strong, tunable, broadband absorption in the visible spectrum, these materials show great promise for applications in solar down-converter technologies. Much subsequent work has been dedicated to uncovering the fundamental mechanisms behind Yb-mediated quantum cutting, and an accumulation of experimental evidence has shown that a particular speciation of Yb, believed to be a fully compensated $(2\mathrm{Yb_{Pb}} + \mathrm{V_{Pb}})^0$ defect complex, dominates this process. In this work, we investigate Yb defect formation in single-crystal $CsPbCl_3$, and in particular the feasibility of forming $(2\mathrm{Yb_{Pb}} + \mathrm{V_{Pb}})^0$ defect complexes, using first-principles electronic structure calculations. A simple thermodynamic model based on defect formation energies, binding energies, and charge transition levels provides some insight into the distribution of $\mathrm{Yb_{Pb}}$ substitutionals and Pb vacancies, underscoring the range of material compositions and synthesis conditions over which locally bound configurations of $(2\mathrm{Yb_{Pb}} + \mathrm{V_{Pb}})^0$ defect complexes become significant. We complement this analysis with additional calculations of structural and electronic properties and discuss the consistency of these results with the observed onset of quantum cutting.

DOI: 10.1103/PhysRevMaterials.6.025404

I. INTRODUCTION

Halide perovskites have garnered massive research interest over the past several years due to a combination of favorable optical and electronic properties and high defect tolerance, leading to promising potential applications in optoelectronic technologies. Nanocrystals (NCs) and thin films of all-inorganic, metal-halide perovskites $CsPbX_3$ (X = Cl, Br, I), in particular, possess a fortunate combination of broadband absorption, narrow emission bandwidths, high photoluminescence quantum yields (PLQYs), and band-gap tunability across the near-infrared (NIR), visible, and ultraviolet (UV) by compositional alloying. Doping by impurity ions has also emerged as a potentially effective route toward engineering additional optical and electronic behavior and controlling perovskite structural stability. Among the myriad possible dopants in $CsPbX_3$, trivalent rare-earth ions (RE^{3+}, e.g., Sc^{3+}, Y^{3+}, Ce^{3+}, Sm^{3+}, Eu^{3+}, Tb^{3+}, Dy^{3+}, Er^{3+}, and Yb^{3+}) stand out in their ability to provide sharp f-f emission features in the visible and NIR.

Surprisingly high PLQYs approaching 200% have recently been achieved in Yb-doped $\mathrm{CsPb(Cl_{1-x}, Br_x)_3}$ [Yb:$\mathrm{CsPb(Cl_{1-x}, Br_x)_3}$] owing to efficient quantum cutting [1–4]. Combined with their strong, broadband absorption in the visible spectrum, these materials are uniquely positioned to act as down-converters for solar technologies. Therefore, it is of particular interest to understand the fundamental mechanisms behind such efficient sensitization of Yb luminescence. Indeed, transient-absorption (TA) spectroscopy in Yb:$CsPbCl_3$ NCs has shown rapid depopulation of photogenerated excitons of the order of a few picoseconds associated with Yb doping [3], in contrast to much slower energy transfer to Yb observed in other quantum cutting materials [1,5–11]. The NIR PLQY was also found to increase with increasingly Cs-rich synthesis conditions [3,4]. Photoluminescence (PL) measurements of $CsPbCl_3$ similarly doped with optically inert La revealed the existence of a shallow, RE^{3+} dopant-induced defect state. Taken together, these observations led Milstein *et al.* to conclude that efficient quantum cutting (i.e., the splitting of a high-energy photon into two low-energy photons) could be mediated by a charge-compensated defect complex $(2\mathrm{Yb_{Pb}} + \mathrm{V_{Pb}})^0$ involving two $\mathrm{Yb_{Pb}^{1+}}$ substitutionals and a Pb vacancy, $\mathrm{V_{Pb}^{2-}}$. In this picture, a shallow $\mathrm{V_{Pb}^{2-}}$ defect rapidly localizes a photogenerated charge carrier, while the spatial proximity of the pair of $\mathrm{Yb_{Pb}^{1+}}$ and large exciton Bohr radius allows for simultaneous electronic coupling with both Yb ions, which serve to split the energy of the localized excitation and reemit a pair of NIR photons.

Subsequent work by Kroupa *et al.* on Yb:$CsPbCl_3$ thin films verified that quantum cutting is not fundamentally tied to the large surface-to-volume ratio of the NCs, but is rather an intrinsic, bulklike property of the material [4]. Using time-resolved PL (TRPL), Roh *et al.* found direct evidence for a shallow dopant-induced defect state acting as an intermediary for quantum cutting in both NCs and single crystals (SCs) of Yb:$CsPbCl_3$ [12]. Furthermore, while the authors inferred the presence of multiple Yb species in both NC and SC samples, the same species was found to dominate quantum cutting in both forms. These studies are largely consistent with the proposal by Milstein *et al.* for the primary role of $(2\mathrm{Yb}_{\mathrm{Pb}} + \mathrm{V}_{\mathrm{Pb}})^0$ defect complexes in mediating quantum cutting, but precise atomistic details of the defect structure remain unknown.

In this work, we further investigate defect formation in single-crystal Yb:$CsPbCl_3$ using first-principles electronic structure calculations. We are interested, in particular, in the feasibility of forming $(2\mathrm{Yb}_{\mathrm{Pb}} + \mathrm{V}_{\mathrm{Pb}})^0$ defect complexes and the extent to which the formation of this complex competes with other speciations of Yb dopants as a function of material composition. First, we identify the low-energy motifs of $\mathrm{Yb}_{\mathrm{Pb}}$-$\mathrm{V}_{\mathrm{Pb}}$ complexes using *ab initio* defect formation energies and binding energies. We provide additional structural characterization by analyzing Yb defect-induced lattice strain and perturbations to local bonding, discussing their consistency with the experimental studies mentioned above [3,4,12]. To understand the distribution of Yb defect speciation under experimentally relevant synthesis conditions, we construct a minimal, self-consistent thermodynamic model for the concentrations of Yb defects as a function of material composition, constrained by the phase stability of $CsPbCl_3$ and parameterized by formation energies. Since variations in material composition are necessarily accompanied by the formation of intrinsic defects, this model also accounts for the formation of intrinsic vacancies, which prior computational studies have identified as the low formation energy defects in $CsPbCl_3$ [13].

Although we identify a motif of $(2\mathrm{Yb}_{\mathrm{Pb}} + \mathrm{V}_{\mathrm{Pb}})^0$ with a specific orientation in the perovskite lattice as having the lowest energy, we find that several configurations of the Yb defect complex are likely to be present at finite temperature. Of specific relevance to quantum cutting is the likelihood of finding two $\mathrm{Yb}_{\mathrm{Pb}}^{1+}$ within a critical radius of a $\mathrm{V}_{\mathrm{Pb}}^{2-}$. Our thermodynamic model shows that the fraction of $\mathrm{V}_{\mathrm{Pb}}^{2-}$ locally coordinated by at least two $\mathrm{Yb}_{\mathrm{Pb}}^{1+}$ generally increases both for increasingly Yb-rich synthesis conditions and for increasing the relative Cs:Pb composition. The increasing incorporation of Yb is also found to decrease the concentration of Cl vacancies, which may otherwise act as nonradiative recombination centers.

Finally, we investigate the role of shallow $\mathrm{V}_{\mathrm{Pb}}^{2-}$ in mediating charge carrier localization prior to quantum cutting, employing a family of effective Hamiltonians to predict bounds on the exciton localization energy and commenting on the potential relevance of large polaron formation. In particular, we find that the inclusion of polaronic effects can, depending on the choice of model, yield good agreement with the experimental PL signatures for RE^{3+} dopant-induced shallow trap emission reported by Milstein *et al.* [3]. However, our polaron-exciton model choice also predicts weaker exciton binding energies compared to reported experimental values. We comment on potential sources of this disagreement and argue for our model's consistency with the observation of lower PLQYs and the absence of exciton PL in SC samples reported by Roh *et al.* [12].

II. RESULTS AND DISCUSSION

A. Formation energies and charge transition levels

In the following, we consider defects in the low-energy, orthorhombic *Pnma* perovskite phase of $CsPbCl_3$ [12,14]. Formation energies E_f of dilute point defects and point defect complexes were calculated from plane-wave, Kohn-Sham density functional theory (DFT) using the supercell approach [15–17], where

$$E_f(d,q) = E(d,q) - E_{\mathrm{bulk}} + \sum_j n_j\left(\mu_j^0 + \Delta\mu_j\right) + q(E_{\mathrm{VBM}} + E_{\mathrm{Fermi}}) + E_{\mathrm{corr}}. \tag{1}$$

Here, $E(d,q)$ is the total energy of the relaxed supercell containing defect d in charge state q and E_{bulk} is the total energy of the perfect supercell. The integer n_j counts the number of chemical species j removed from ($n_j > 0$) or added to ($n_j < 0$) the system in forming the defect. The synthesis conditions are characterized by the chemical potentials $\Delta\mu_j$ with respect to a set of standard references μ_j^0, which we take to be the elemental solid phases of Cs and Pb and the Cl_2 molecule. Analogously, the Fermi level E_{Fermi} is referenced to the valence band maximum (VBM) of the bulk supercell. A finite-size correction term E_{corr} has been added to account for spurious Coulomb interactions between the point defect and its periodic images, derived according to the charge correction scheme proposed by Freysoldt, Neugebauer, and Van de Walle (FNV) [18]. Since the defect complexes considered in this work span multiple Pb-sublattice sites, all defect calculations were performed on a fairly large supercell containing 360 atoms (a 3 × 3 × 2 supercell of the 20-atom *Pnma* unit cell). Appendix A contains additional computational details. Assuming the stability of $CsPbCl_3$ against secondary phase formation provides additional constraints on the set of primary chemical potentials,

$$x\Delta\mu_{\mathrm{Cs}} + y\Delta\mu_{\mathrm{Pb}} + z\Delta\mu_{\mathrm{Cl}} \leqslant \Delta H_f(\mathrm{Cs}_x\mathrm{Pb}_y\mathrm{Cl}_z), \tag{2}$$

where $\Delta H_f(\mathrm{Cs}_x\mathrm{Pb}_y\mathrm{Cl}_z)$ are the formation enthalpies of the relevant primary and secondary phases, and the equality is strictly satisfied for the primary phase $CsPbCl_3$, $x = y = 1$, and $z = 3$. In addition to the elemental references noted above, we calculated the formation enthalpies of CsCl, $PbCl_2$, Cs_2PbCl_6, and Cs_4PbCl_6. The corresponding phase-stability diagram (Fig. 1) shows a narrow existence range for $CsPbCl_3$.

Previous first-principles studies of native point defects in $CsPbX_3$ perovskites (X = Cl, Br, I) have found low formation energies for vacancies over a wide set of processing conditions [13]. Likewise, ample experimental evidence points to the incorporation of Yb via B-site cation substitution [1–3,12,19,20], so Yb incorporation is only assumed to occur by substituting Pb sites. The Yb chemical potential is

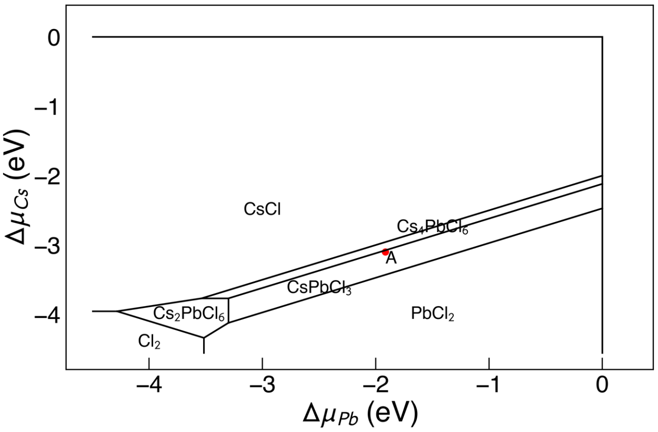

FIG. 1. Predicted phase-stability diagram for $\mathrm{CsPbCl_3}$. Chemical potentials chosen at point A reflect moderately Pb-poor, Cs-rich synthesis conditions used in calculating defect formation energies shown in Fig. 2.

chosen to be consistent with experimentally observed Yb composition, [Yb]/([Yb]+[Pb]) [3]. Furthermore, it has been observed that the facile incorporation of Yb occurs under moderately Pb-poor and Cs-rich conditions. Since the Cs chemical potential is tightly constrained by phase stability (Fig. 1), we choose Pb chemical potentials which are far below the pure Pb secondary phase boundary and consistent with observed Yb compositions and nominal [Cs]/[Pb] ratios [3], [Yb]/([Yb]+[Pb]) <0.1 and 1.0 ⩽ [Cs]/[Pb] <1.4.

From preliminary calculations of a variety of charge-neutral defect complexes involving $\mathrm{Yb}_{\mathrm{Pb}}^{1+}$ compensated by either cation vacancies $\mathrm{V}_{\mathrm{Cs}}^{1-}$ and $\mathrm{V}_{\mathrm{Pb}}^{2-}$ or halide interstitials $\mathrm{Cl}_{\mathrm{i}}^{1-}$, we found that $(2\mathrm{Yb}_{\mathrm{Pb}}+\mathrm{V}_{\mathrm{Pb}})^0$ consistently had the lowest formation energy for synthesis conditions within the bounds of phase stability. In particular, we considered $(2\mathrm{Yb}_{\mathrm{Pb}}+2\mathrm{Cl}_{\mathrm{i}})^0$, $(2\mathrm{Yb}_{\mathrm{Pb}}+2\mathrm{V}_{\mathrm{Cs}})^0$, and $(2\mathrm{Yb}_{\mathrm{Pb}}+\mathrm{V}_{\mathrm{Cs}}+\mathrm{Cl}_{\mathrm{i}})^0$ as alternative fully compensated complexes to $(2\mathrm{Yb}_{\mathrm{Pb}}+\mathrm{V}_{\mathrm{Pb}})^0$. For the range of chemical potential consistent with facile Yb incorporation, the formation energy of $(2\mathrm{Yb}_{\mathrm{Pb}}+\mathrm{V}_{\mathrm{Pb}})^0$ was lower than the other fully compensated complexes by at least 1 eV. This provides additional justification for treating vacancies as the dominate intrinsic defects in our models, and thus the following analyses focus on complexes involving only $\mathrm{Yb}_{\mathrm{Pb}}^{1+}$ and $\mathrm{V}_{\mathrm{Pb}}^{2-}$.

The computed formation energies of vacancies, $\mathrm{Yb}_{\mathrm{Pb}}$, and $\mathrm{Yb}_{\mathrm{Pb}}+\mathrm{V}_{\mathrm{Pb}}$ complexes are shown in Fig. 2 for one choice of moderately Pb-poor, Cs-rich synthesis conditions (point A in Fig. 1). Table I lists the corresponding thermodynamic charge transition levels,

$$\varepsilon(q_1|q_2)=\frac{E_f(d,q_1)|_{E_{\mathrm{Fermi}}=0}-E_f(d,q_2)|_{E_{\mathrm{Fermi}}=0}}{q_2-q_1}. \quad (3)$$

It is worth emphasizing that the thermodynamic charge transition levels are independent of the chemical potentials. Furthermore, since the ground state of the defect in a given charge state includes geometry relaxation in defining the formation energy, Eq. (3) implicitly assumes the defect geometry has sufficient time to equilibrate upon changing the charge state.

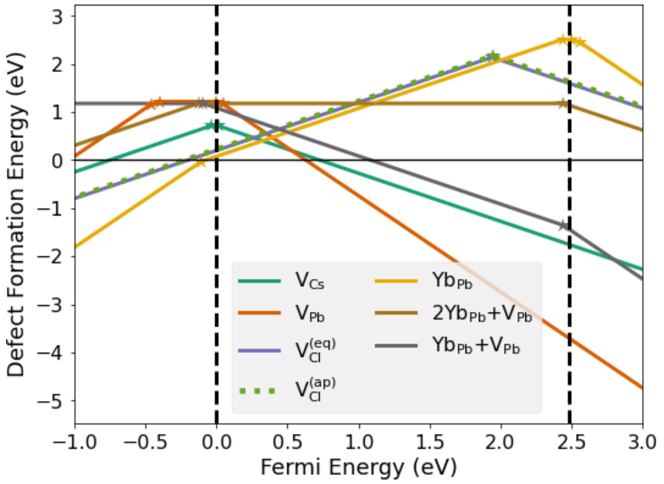

FIG. 2. DFT formation energies of vacancies, $\mathrm{Yb}_{\mathrm{Pb}}$ substitutionals, and vacancy-substitutional complexes in moderately Pb-poor $\mathrm{CsPbCl_3}$. Chemical potentials correspond to point A in Fig. 1. The DFT band gap, $E_{\mathrm{gap}}=2.48$ eV, is demarcated by dashed vertical lines. The difference in formation energy between Cl vacancies at symmetrically distinct apical (ap) and equatorial (eq) is very small.

We find that the cation vacancies $\mathrm{V_{Cs}}$ and $\mathrm{V_{Pb}}$ introduce shallow acceptor levels near the VBM. Conversely, an isolated $\mathrm{Yb_{Pb}}$ acts as a shallow donor, with a series of thermodynamic charge transition levels near the conduction band minimum (CBM), each separated by ≈60 meV (Table I). Interestingly, $2\mathrm{Yb}_{\mathrm{Pb}}+\mathrm{V}_{\mathrm{Pb}}$ and $\mathrm{Yb}_{\mathrm{Pb}}+\mathrm{V}_{\mathrm{Pb}}$ complexes create, respectively, very deep $(0|-1)$ and $(-1|-2)$ acceptor levels near the CBM. Thus, $\mathrm{Yb_{Pb}}$ substitutionals, whether bound or unbound to Pb vacancies, introduce single-particle, Kohn-Sham states resonant within the conduction band. These defect-localized states (DLS) are typically associated with the existence of an effective-mass-like, perturbed-host state slightly below the conduction band; the latter effective-mass state is generally not observable in supercell calculations due to finite-size constraints [17,21,22]. For isolated $\mathrm{Yb_{Pb}}$, this picture is consistent with its shallow donor character. Adding a Pb vacancy introduces coupling to the valence band via Cl dangling bonds [23]. For fully compensated $2\mathrm{Yb}_{\mathrm{Pb}}+\mathrm{V}_{\mathrm{Pb}}$ complexes, this stabilizes the neutral charge state throughout most of the band gap. It is possible that the isolated $(0|-1)$ acceptor state

TABLE I. Thermodynamic charge transition levels relative to VBM. For reference, the DFT band gap is $E_{\mathrm{gap}}=2.48$ eV, and intraband states within 0.1 eV to band edges are also included.

Defect	$\varepsilon(q_1\|q_2)$ (eV)
$2\mathrm{Yb}_{\mathrm{Pb}}+\mathrm{V}_{\mathrm{Pb}}$	2.438 $(0\|-1)$
$\mathrm{Yb}_{\mathrm{Pb}}+\mathrm{V}_{\mathrm{Pb}}$	−0.093 $(0\|-1)$, 2.440 $(-1\|-2)$
$\mathrm{Yb}_{\mathrm{Pb}}$	2.435 $(1\|0)$, 2.497 $(0\|-1)$, 2.559 $(-1\|-2)$
V_{Pb}	0.005 $(-1\|0)$, 0.045 $(-1\|-2)$
V_{Cs}	−0.038 $(1\|0)$, 0.013 $(0\|-1)$
$\mathrm{V}_{\mathrm{Cl}}^{(\mathrm{ap})}$	1.945 $(+1\|-1)$
$\mathrm{V}_{\mathrm{Cl}}^{(\mathrm{eq})}$	1.939 $(+1\|-1)$

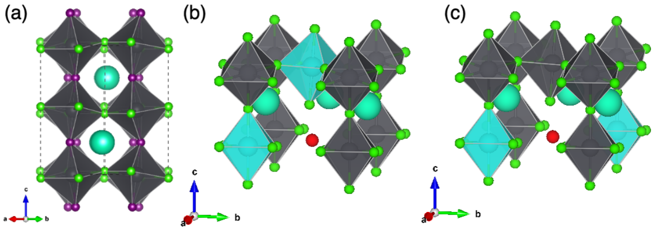

FIG. 3. (a) Symmetrically distinct apical (purple) and equatorial (green) Cl sites associated with Pb-Cl octahedral (gray) tilting in the 20-atom unit cell of the *Pnma* perovskite phase of $CsPbCl_3$. (b) Orthogonal OT $[110]^{\perp}$ and (c) collinear CL [110] motifs of the $(2Yb_{Pb} + V_{Pb})^0$ complex, where Yb-Cl octahedra (teal) are first-nearest neighbors to a vacant Pb site (red).

close to the CBM corresponds to the Yb dopant-induced intermediate state proposed as essential to sensitizing efficient quantum cutting [3,12]. However, it is difficult to resolve the accuracy of DFT formation energies and transition levels below ≈50 meV [17]; the presence of this transition level may simply reflect the filling of bulk conduction band states.

We find very little difference in formation energies between Cl vacancies at symmetrically distinct apical (ap) and equatorial (eq) Cl sites (Fig. 3). These vacancies form somewhat deep amphoteric defect states with negative-U behavior [24] and may act as nonradiative recombination centers [25,26]. This negative-U behavior is accompanied by large relaxation in the distance between neighboring Pb in the $[PbCl_5]$ octahedra sharing a V_{Cl}^{1-} at their adjacent corner. The resulting formation of a contracted Pb-Pb dimer and the bonding character of Pb p orbitals shifts the V_{Cl}^{1-} DLS into the band gap [23,27]. It would be interesting to determine whether Cl vacancies can exhibit metastable behavior under photoexcitation [28,29], particularly in light of the observation made by Roh *et al.* of slow quantum cutting due to metastable trapping states and lower PLQYs in SC samples [12]. However, it is worth noting that due to the stability constraints on $CsPbCl_3$ (Fig. 1), increasingly Pb-poor synthesis conditions approach Cl-rich secondary phase boundaries and would thus disfavor the formation of Cl vacancies. For the conditions depicted in Fig. 2, compensation between positively charged V_{Cl}^{1+} and Yb_{Pb}^{1+} and negatively charged V_{Pb}^{2-} and V_{Cs}^{1-} pins the Fermi level at about 0.4 eV above the VBM.

To gain some insight into whether $Yb_{Pb} + V_{Pb}$ complexes can form in sufficient concentrations to contribute to quantum cutting and high PLQYs, we tabulate (Table II) binding energies for $(Yb_{Pb} + V_{Pb})^{1-}$ and $(2Yb_{Pb} + V_{Pb})^0$ complexes in symmetrically distinct configurations. We define the binding energy as the difference between the formation energy of the complex, c, and the sum of the formation energies of the individual, isolated point defects, d,

$$E_{\text{bind}} = E_f(c, q_c) - \sum_{d \in c} E_f(d, q_d). \qquad (4)$$

Note that this is in contrast to the other commonly used definition, where the energy of the complex is referenced to a single point defect and a complementary subcomplex. Moreover, since the constituent defects, Yb_{Pb} and V_{Pb}, and their complexes are shallow, the formation energies in (4) are taken to be in the nominal defect-charge states. Hence, the binding energies in Table II are independent of the Fermi level. Among $(Yb_{Pb} + V_{Pb})^{1-}$ complexes, the [001] orientation is marginally energetically favorable. In contrast, among the collinear (CL) $(2Yb_{Pb} + V_{Pb})^0$ configurations, the [110] orientation is favorable. The lowest-energy $(2Yb_{Pb} + V_{Pb})^0$ configuration is found for an orthogonal (OT) motif, where the vector perpendicular to the plane spanned by the complex lies in the [110] direction, denoted by $[110]^{\perp}$ (cf. Table II). Restricting to the minimum energy $(Yb_{Pb} + V_{Pb})^{1-}$ [001] complex, we find that about 0.13 eV is gained upon adding another Yb_{Pb}^{1+} to form a $(2Yb_{Pb} + V_{Pb})^0$ OT $[110]^{\perp}$ complex. That the OT motifs are marginally more stable than CL motifs is contrary to what one would expect based on simple electrostatic interactions between the constituent point defects, suggesting that lattice strain among the different configurations plays a nontrivial role. A similar claim was made by Li *et al.* for $(2Yb_{Pb} + V_{Pb})^0$ complexes in the cubic perovskite phase of $CsPbCl_3$, who argued that the number of neighboring, distorted Pb-Cl octahedra differentiate OT and CL motifs [30]. The magnitudes of the complex binding energies relative to $k_B T$ indicate relative favorability for the formation of all complex motifs at room temperature. We consider simple

TABLE II. Binding energies E_{bind} of vacancy-substitutional defect complexes, local $[YbCl_6]$ symmetry, relaxed defect volume V_{def} from DFT relative to bulk volume V_0, and symmetry-adapted components e_i of the Green-Lagrange strain tensor with respect to a relaxed, bulk $CsPbCl_3$ lattice. The largest absolute values of the strain components in the defect set are highlighted in italics. Lattice orientations of the defect complexes are specified by $[\cdots]$, where $[\cdots]^{\perp}$ denotes the vector perpendicular to the plane spanned by an orthogonal (OT) complex.

Defect complex	E_{bind} (eV)	Yb Site Sym.	V_{def}/V_0	e_1 (10^{-3})	e_2 (10^{-3})	e_3 (10^{-3})	e_4 (10^{-3})	e_5 (10^{-3})	e_6 (10^{-3})
$(2Yb_{Pb} + V_{Pb})^0$ CL [110]	−0.308	D_{2h}	0.994	−3.323	−1.670	−6.490	*−0.503*	0.027	0.328
$(2Yb_{Pb} + V_{Pb})^0$ CL [001]	−0.278	O_h	0.994	−3.199	−2.631	−4.966	0.087	*−0.347*	*−2.096*
$(2Yb_{Pb} + V_{Pb})^0$ OT $[110]^{\perp}$	−0.340	D_{2h}, C_s	0.994	−3.172	−2.006	−6.004	−0.314	−0.149	1.174
$(2Yb_{Pb} + V_{Pb})^0$ OT $[001]^{\perp}$	−0.315	D_{2h}	0.994	−3.214	−1.873	−6.758	0.016	−0.232	0.388
$(Yb_{Pb} + V_{Pb})^{1-}$ [110]	−0.190	D_{2h}	1.000	−0.231	−2.136	−6.900	−0.294	0.001	0.787
$(Yb_{Pb} + V_{Pb})^{1-}$ [001]	−0.207	D_{2h}	1.000	−0.156	−2.617	−6.179	0.084	−0.060	−1.432
${Yb_{Pb}}^{1+}$		O_h	*0.992*	*−4.626*	*−3.446*	−5.501	0.034	−0.126	−0.370
${V_{Pb}}^{2-}$			*1.005*	2.916	−2.714	*−6.951*	0.029	0.068	1.160

thermodynamic models of the defect distributions based on the formation energies in Sec. II C.

B. Structural characterization

The formation of V_{Pb}^{2-}, Yb_{Pb}^{1+} and their complexes is accompanied by a certain amount of lattice strain. To quantify the degree of strain induced by defect formation, we calculate the deformation matrix $\mathbf{F}$ of the pristine bulk lattice $\mathbf{L}_0$ which produces the relaxed, defective supercell lattice $\mathbf{L}_1$, where

$$\mathbf{L}_1 = \mathbf{F}\mathbf{L}_0. \tag{5}$$

A generalized, one-parameter family of strain tensors can be defined by [31]

$$\mathbf{E}(\mu) = \frac{(\mathbf{F}^\top\mathbf{F})^\mu - \mathbf{I}}{2\mu}, \tag{6}$$

where the typical Green-Lagrange strain is given by $\mu = 1$. In Table II, we have tabulated the symmetry-adapted components e_i [Eqs. (7)–(12)] of the Green-Lagrange strain tensor for V_{Pb}^{2-}, Yb_{Pb}^{1+} and their complexes [31]:

$$e_1 = (E_{xx} + E_{yy} + E_{zz})/\sqrt{3}, \tag{7}$$

$$e_2 = (E_{xx} - E_{yy})/\sqrt{2}, \tag{8}$$

$$e_3 = (2E_{zz} - E_{xx} - E_{yy})/\sqrt{6}, \tag{9}$$

$$e_4 = \sqrt{2}E_{yz}, \tag{10}$$

$$e_5 = \sqrt{2}E_{xz}, \tag{11}$$

$$e_6 = \sqrt{2}E_{xy}. \tag{12}$$

The first component of the Green-Lagrange strain, e_1, characterizes purely volumetric contraction or expansion of the lattice. Volume-preserving, deviatoric strains are spanned by e_2 and e_3, while shear strains are given by e_4, e_5, and e_6. We note that the magnitudes of the strain components (Table II) are small enough that they are well approximated by the linearized strain, $\mathbf{E} \approx \frac{1}{2}(\mathbf{F} + \mathbf{F}^\top) - \mathbf{I}$.

We find that the largest volume changes occur for the isolated defects V_{Pb}^{2-} and Yb_{Pb}^{1+}, where the lattice expands in forming the vacancy and contracts for the substitutional. Remarkably, we find no significant volume change for the $(Yb_{Pb} + V_{Pb})^{1-}$ complexes, suggesting that the volumetric strains of the constituent point defects essentially compensate each other. This may provide some explanation for the conspicuous absence of differences in lattice parameters in x-ray diffraction (XRD) data between undoped and Yb-doped $CsPbX_3$ NCs and SCs [3,4,12,32–35]. To further investigate this observation, we invoke a simple thermodynamic model for the defect-perturbed lattice volume V_{def} as a function of defect concentrations $c_{d,q}$,

$$V_{def} = V_0 + \sum_{d,q} c_{d,q}v_{d,q} + n_h v_h + n_e v_e, \tag{13}$$

where $v_{d,q} = p_{d,q}V_0/B_0$ is the partial volume of defect d in charge state q, B_0 is the bulk modulus (≈23.0 GPa), and V_0 is the bulk volume [36]. An effective defect pressure is defined by the change in the DFT total energy of the defect supercell during volume relaxation [36,37],

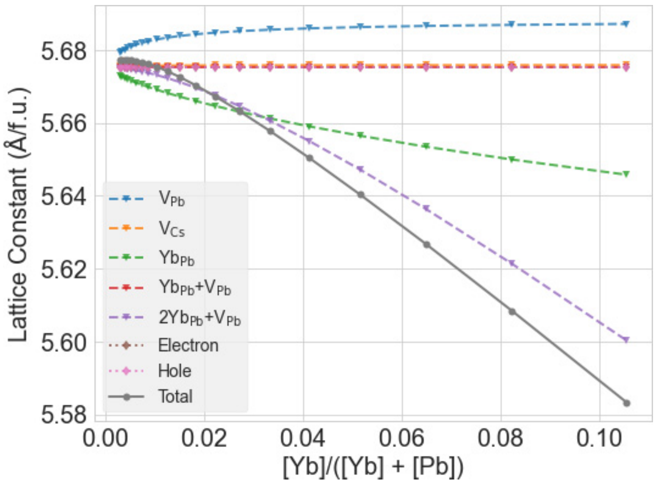

FIG. 4. Total change in pseudocubic lattice constant $a_{def} = V_{def}^{1/3}$ per formula unit (f.u.) due to Yb doping and defect formation, where V_{def} is given by (13). Individual contributions to a_{def} from each defect and free electrons and holes are also shown.

$$p_{d,q} = -\frac{\Delta[E_{d,q}(V) - E_{bulk}(V)]}{\Delta V}, \tag{14}$$

where the difference, $\Delta(\cdot) = (\cdot)|_{V=V_{def}} - (\cdot)|_{V=V_0}$, is evaluated at the relaxed V_{def} and unrelaxed V_0 DFT cell volumes. To account for volume changes associated with the introduction of free charge carriers consistent with overall charge neutrality (17), we augment Eq. (13) by the partial volumes $v_{e,h}$ of free electrons and holes introduced into bulk $CsPbCl_3$, with respective concentrations $n_{e,h}$. In this case, the free electron and hole volumes are derived from relaxed bulk supercells following, respectively, the addition or removal of an electron.

Using the model for defect concentrations (16), discussed in Sec. II C, Fig. 4 shows that the predicted contraction of the effective lattice constant $a_{def} = V_{def}^{1/3}$ is less than 0.1 Å for Yb incorporation within the experimentally relevant range. For less than 2% Yb incorporation, the lattice constant is reduced by less than 0.1% relative to the unperturbed value $a_0 = V_0^{1/3}$, limited primarily by the compensation in volumetric strain between V_{Pb}^{2-} and Yb_{Pb}^{1+}. For higher Yb incorporation, the change in the lattice constant becomes dominated by the formation of $(2Yb_{Pb} + V_{Pb})^0$ complexes, but the overall change relative to the bulk is less than 1.8%. Moreover, extensive charge compensation between V_{Pb}^{2-}, Yb_{Pb}^{1+}, and $(Yb_{Pb} + V_{Pb})^{1-}$ also limits the contribution of free charge carriers to the volume deformation, which only reach concentrations of the order of 10^{10}–10^{12} cm^{-3} under the experimental synthesis conditions considered here (cf. Sec. II C).

To some extent, the differences in binding energies among the configurations of the $(2Yb_{Pb} + V_{Pb})^0$ complexes can be understood from the local distortion of Pb-Cl bond lengths near the Yb_{Pb}^{1+} and the distribution of Green-Lagrange strain components. In the pristine *Pnma* perovskite phase, the average predicted Pb-Cl bond length is 2.89 Å, while a single Yb_{Pb}^{1+} dopant forms contracted 2.62 Å bonds with surrounding Cl, leading to increased Pb-Cl bond lengths at the shared

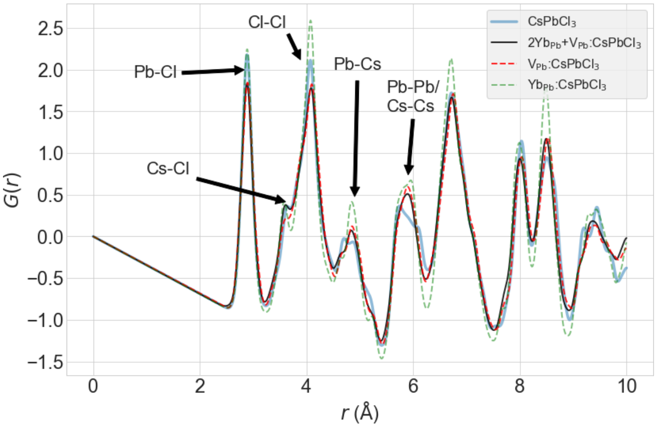

FIG. 5. Reduced pair distribution functions from room-temperature MD simulations of 360-site defect and bulk supercells. Supercells containing an isolated $\mathrm{Yb_{Pb}}$ and a compensated $(2\mathrm{Yb_{Pb}} + \mathrm{V_{Pb}})^0$ complex correspond to Yb fractions, [Yb]/([Yb] + [Pb]), of 1.4% and 2.8%, respectively. The first several features are labeled by the dominant pairs of lattice sites involved.

corners of neighboring Pb-Cl octahedra. That the pairing of two $\mathrm{Yb_{Pb}^{1+}}$ with a $\mathrm{V_{Pb}^{2-}}$ is no longer compensated in volumetric strain (Table II) compared to $(\mathrm{Yb_{Pb}} + \mathrm{V_{Pb}})^{1-}$ complexes follows from the additional set of contracted $\mathrm{Yb_{Pb}}$-Cl bonds. We also note that among the $(2\mathrm{Yb_{Pb}} + \mathrm{V_{Pb}})^0$ motifs, the lower-energy OT configurations induce smaller amounts of xz- and yz-shear strain. Finally, let us mention that the presence of a neighboring Pb vacancy reduces the $\mathrm{Yb_{Pb}}$ orthorhombic site symmetry, from O_h for isolated $\mathrm{Yb_{Pb}^{1+}}$, to $D_{2\mathrm{h}}$ (Table II). This is largely consistent with the spectroscopic analysis reported by Roh *et al.* [12]. It is interesting to note that one Yb in the lowest-energy configuration $(2\mathrm{Yb_{Pb}} + \mathrm{V_{Pb}})^0$ OT $[110]^\perp$ exhibits an additional reduction to reflection site symmetry, C_s.

To investigate finite-temperature effects on bonding, we performed room-temperature molecular dynamics (MD) simulations of the pristine and defective 360-site supercells and extracted the reduced pair distribution function (rPDF), $G(r)$:

$$G(r) = 4\pi r\langle n\rangle(g(r) - 1), \tag{15}$$

where $\langle n\rangle$ is the average number density of atoms, and $g(r) = \sum_{j\neq k}\langle\delta(r - r_{jk})\rangle/(\langle n^2\rangle\Omega)$ is the pair distribution function (PDF). The brackets $\langle\cdot\rangle$ denote an ensemble average over the MD trajectories, $r_{j,k}$ is the distance between atoms j and k, and Ω is the supercell volume.

In Fig. 5, we compare the simulated rPDF for the ensemble of $(2\mathrm{Yb_{Pb}} + \mathrm{V_{Pb}})^0$ complexes against the bulk reference system and supercells containing either a $\mathrm{V_{Pb}^{2-}}$ or a $\mathrm{Yb_{Pb}^{1+}}$. We find that the broadening observed in the rPDF of the $(2\mathrm{Yb_{Pb}} + \mathrm{V_{Pb}})^0$ system is primarily due to the presence of the Pb vacancy. This can be qualitatively understood by invoking a harmonic approximation for the vibrational modes of the lattice: a vacant Pb site is expected to locally reduce the curvature of the Born-Oppenheimer energy landscape, which introduces lower-frequency modes and increases the variance of the pair distribution function. Conversely, sharper features in the rPDF of isolated $\mathrm{Yb_{Pb}^{1+}}$ are likely due to the shortened Yb-Cl bonds and induced lattice contraction. Interestingly, rPDF features involving Cs provide the clearest distinctions among the four systems. Previous computational works have identified the key role played by displacements of A-site cations in ABX_3 halide perovskites in stabilizing the orthorhombic *Pnma* phase [38,39]. Moreover, the low-temperature instability of the cubic perovskite structure to [BX_6] octahedral tilting is often attributed to the presence of an undersized A-site cation; Bechtel and Van der Ven, as well as Young and Rondinelli, found that the tilting mode toward *Pnma* symmetry minimized unfavorable electrostatic interactions and increased A-X covalency by allowing A-site cations to displace from their ideal cubic positions [38,39]. The presence of $\mathrm{Yb_{Pb}}$ substitutionals and Pb vacancies provides additional strain-induced distortions to the volumes of the cuboctahedral voids containing Cs, thereby perturbing the local energy surfaces associated with Cs rattling modes. Whether doping by Yb alters structural phase transitions in halide perovskites, as has been argued for $\mathrm{Bi^{3+}}$ and $\mathrm{Ni^{2+}}$ doping [37,40], is a question we leave for potential future work.

C. Defect complex formation

In this section, we discuss a simple model for the concentration of Yb defects and defect complexes based on the DFT data summarized in Sec. II A. Again, we take as our starting point the set of native vacancies, $\mathrm{Yb_{Pb}}$, and $\mathrm{Yb_{Pb}} + \mathrm{V_{Pb}}$ complexes. For a given choice of chemical potentials and temperature, equilibrium defect concentrations are estimated by the standard Arrhenius relation in the dilute approximation [17],

$$c_{d,q}(\Delta\mu_i, E_\mathrm{Fermi}, T) = g\exp\left[-E_f(q,d)/k_\mathrm{B}T\right], \tag{16}$$

where the formation energy $E_f(q,d)$ is given by Eq. (1) and g is a degeneracy factor accounting for internal and configurational degrees of freedom of the defect. The Fermi level is determined self-consistently by enforcing overall charge neutrality,

$$\sum_{d,q} q c_{d,q} + n_h - n_e = 0, \tag{17}$$

where n_h and n_e are the concentrations of the free hole and electrons, respectively. The free carrier concentration can be obtained either by a Fermi integral over the electronic density of states or in an isotropic, parabolic band approximation with electron and hole effective masses $m^*_{e,h}$ (Table III).

As discussed in Sec. II A, given the tight stability constraints on the Cs chemical potential, we choose chemical potentials of Yb and Pb to be consistent with empirical Yb compositions and nominal Cs:Pb ratios, focusing specifically on moderately Pb-poor synthesis conditions. Figure 6 shows the defect concentrations and self-consistent Fermi level for increasing Yb chemical potential, where the Cs and Pb chemical potentials remain fixed at point A in the phase-stability diagram (Fig. 1). The formation of $\mathrm{Yb_{Pb}^{1+}}$ defects leads to charge compensation by negative cation vacancies $\mathrm{V_{Pb}^{2-}}$ and $\mathrm{V_{Cs}^{1-}}$. A reduction in $\mathrm{V_{Cl}^{1+}}$ and the increasing concentration of (partially) compensated $(\mathrm{Yb_{Pb}} + \mathrm{V_{Pb}})^{1-}$ and $(2\mathrm{Yb_{Pb}} + \mathrm{V_{Pb}})^0$ complexes further leads to a slight increase in the Fermi

TABLE III. Electron and hole effective masses $m^*_{e,h}$, and static and high-frequency dielectric constants ϵ_s, ϵ_∞, in cubic and orthorhombic phases of $CsPbCl_3$ from density functional perturbation theory. The exciton binding energies E_X and effective Bohr radii a^*_B are predicted from the Wannier-Mott model (24) and (25). The variational ground-state energy E_{GS} of the defect-bound exciton relative to E_X and the expected exciton radius $\langle r_{12}\rangle$ are determined by the same weakly screened electron-hole potential $V(r_{12}) \propto 1/\epsilon_\infty r_{12}$. Approximate phonon screening corrections ΔE_X, accounting for (neglecting) parabolic electron band dispersion [60], are also shown.

Phase	m^*_h	m^*_e	ϵ_∞	ϵ_s	E_X (meV)	a^*_B (nm)	ΔE_X (meV)	$E_{GS} - E_X$ (meV)	$\langle r_{12}\rangle$ (nm)
$Pm\bar{3}m$ (cubic)	0.17	0.18	4.08	20.56	71.7	2.46	−17.1 (−30.6)	63.7	2.08
Pnma (ortho)	0.25	0.26	4.09	23.67	103.0	1.70	−18.6 (−34.4)	78.9	1.19

level for sufficient Yb incorporation. It is worth noting that previous experimental work found that doping by trivalent lanthanide cations suppressed the formation of Cl vacancies, which agrees with our model prediction [41].

Since Milstein *et al.* found that NIR PLQY increased with increasingly Cs-rich synthesis conditions [3], we also assess the extent to which controlling the relative chemical potentials of Cs and Pb influences the formation of Yb complexes. Figure 7 shows the estimated distribution of various spatial configurations of Yb^{1+}_{Pb} relative to V^{2-}_{Pb} (see below) for increasing [Cs]/[Pb] with fixed, relatively favorable Yb and Cl chemical potentials. We found that the effect of increasingly Cs-rich, Pb-poor synthesis conditions within the bounds set by phase stability is essentially identical to controlling the Yb chemical potential. Hence, Fig. 7 also shows the equivalent change in Yb fraction, [Yb]/([Yb] + [Pb]). In particular, decreasing the Pb chemical potential increases both the concentration of Pb vacancies and Yb_{Pb}, and increasing the Cs chemical potential disfavors the formation of Cs vacancies. The ensuing charge compensation between Yb^{1+}_{Pb} and V^{2-}_{Pb} and their increasing concentrations lead to the formation of $(2Yb_{Pb} + V_{Pb})^0$ complexes.

The binding energy calculations of Sec. II A (Table II) indicate that several motifs of the $(2Yb_{Pb} + V_{Pb})^0$ complex should be expected at room temperature; entropic considerations suggest that an ensemble of partially dissociated configurations of Yb^{1+}_{Pb} and V^{2-}_{Pb} should also be present. Furthermore, while the static dielectric constant ϵ_s of $CsPbCl_3$ is relatively large, the Debye length scale is of the order of the effective exciton Bohr radius a^*_B for the self-consistently determined free carrier concentrations. Hence, some degree of screened Coulomb attraction between Yb^{1+}_{Pb} and V^{2-}_{Pb} should additionally bias the distribution of Yb toward partially bound configurations within a^*_B, which may be important for quantum cutting. To characterize the spatial distribution of Yb relative to Pb vacancies, we assume pairwise interactions between point defects in the form of a screened Coulomb

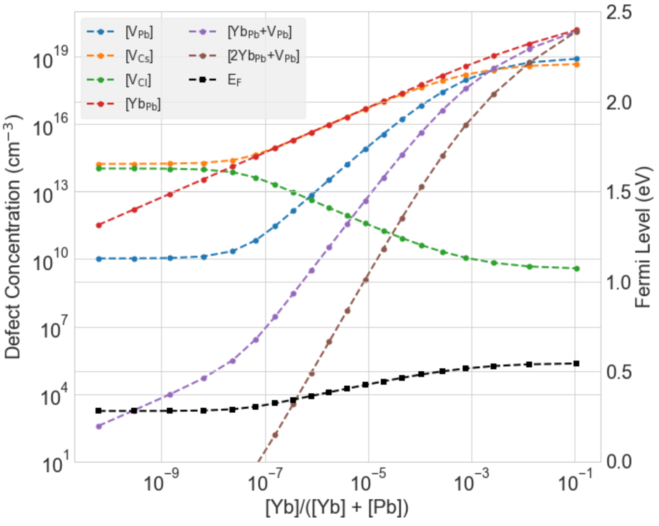

FIG. 6. Room-temperature defect concentrations and self-consistent Fermi level for increasing Yb incorporation with fixed Cs and Pb chemical potentials.

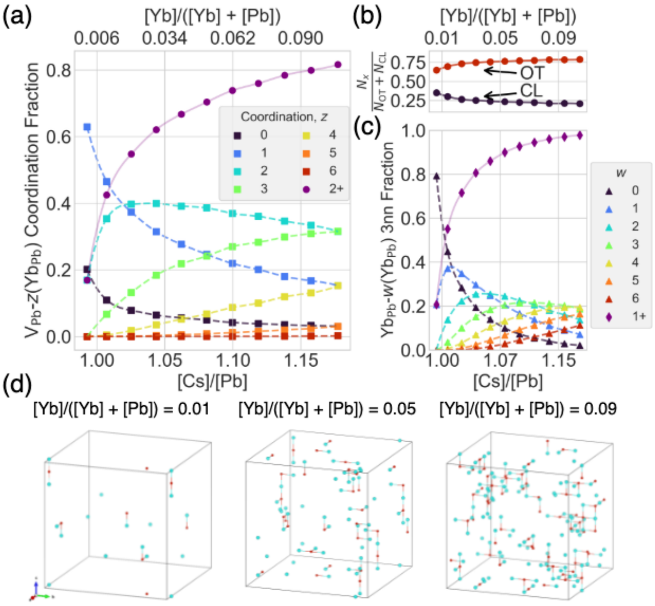

FIG. 7. Data from room-temperature Monte Carlo simulation: (a) Fraction of V^{2-}_{Pb} coordinated by z Yb^{1+}_{Pb} at first-nearest-neighbor (1NN) positions (Pb sublattice) for increasing relative Cs:Pb composition, [Cs]/[Pb]. The equivalent change in Yb fraction, [Yb]/([Yb] + [Pb]), is shown on the top axis. The fraction of V^{2-}_{Pb} coordinated by at least two Yb^{1+}_{Pb} is labeled "2+". (b) Composition dependence of the relative fraction $N_x/(N_{OT} + N_{CL})$ of OT and CL configurations of the $2Yb_{Pb} + V_{Pb}$ complex, where N_x is the average number of complexes with configurational motif x = OT or CL. (c) Fraction of Yb^{1+}_{Pb} with w Yb^{1+}_{Pb} within third-nearest-neighbor (3NN) distance (Pb sublattice). Fractions of Yb substitutionals with $w > 6$ are not shown for clarity. The fraction of Yb^{1+}_{Pb} with at least one other Yb^{1+}_{Pb} within 3NN is labeled "1+". (d) Equilibrium snapshots of V^{2-}_{Pb} (red) and Yb^{1+}_{Pb} (teal) configurations in the MC simulation cell for increasing Yb fraction. Edges connecting V^{2-}_{Pb} and Yb^{1+}_{Pb} at 1NN positions on the Pb sublattice are also shown.

potential $\phi(r) \propto \exp(-r/L_\mathrm{D})/(\epsilon_s r)$. The Debye length was determined by the self-consistent free carrier concentrations $L_\mathrm{D} = \sqrt{\epsilon_s \epsilon_0 k_\mathrm{B} T/[e^2(n_e + n_h)]}$, and the static dielectric constant was calculated using density functional perturbation theory (Table III). It is important to note that while this model introduces errors in reproducing the DFT binding energies of local motifs (Table II) of the order of $k_\mathrm{B}T$ at room temperature, it is within the expected accuracy of DFT formation energies [17]. Equilibrium spatial configurations of $\mathrm{Yb}_\mathrm{Pb}^{1+}$ and $\mathrm{V}_\mathrm{Pb}^{2-}$ were sampled using Metropolis Monte Carlo (MC) in the canonical ensemble.

Fast rise times observed by Roh *et al.* in TRPL measurements support the hypothesis that efficient quantum cutting in Yb:$\mathrm{CsPbCl_3}$ depends on short-range, Dexter-type exchange-mediating energy transfer between dopant-induced $\mathrm{V}_\mathrm{Pb}^{2-}$ and nearby $\mathrm{Yb}_\mathrm{Pb}^{1+}$ [3,12,42]. Since such an exchange mechanism is typically short range and would rely on sufficient wavefunction overlap between Yb pairs, configurations of $\mathrm{V}_\mathrm{Pb}^{2-}$ and at least two $\mathrm{Yb}_\mathrm{Pb}^{1+}$ in which each $\mathrm{Yb}_\mathrm{Pb}^{1+}$ is within the first-nearest-neighbor (1NN) shell on the Pb sublattice relative to the $\mathrm{V}_\mathrm{Pb}^{2-}$ are likely most relevant for quantum cutting. Hence, in Fig. 7, we characterize the local Yb environment surrounding the Pb vacancies predicted by room-temperature MC simulation.

Figure 7(a) shows that for very dilute ($\ll 1\%$) Yb incorporation, Pb vacancies are predominantly isolated or bound in partially compensated $(\mathrm{Yb_{Pb}} + \mathrm{V_{Pb}})^{1-}$ complexes. From there, small increases in the Yb fraction lead to the rapid formation of fully compensated $(2\mathrm{Yb_{Pb}} + \mathrm{V_{Pb}})^0$ complexes, while depopulating the relative fraction of free Pb vacancies and $(\mathrm{Yb_{Pb}} + \mathrm{V_{Pb}})^{1-}$ complexes. The relative proportion of Pb vacancies coordinated by exactly two $\mathrm{Yb}_\mathrm{Pb}^{1+}$ peaks around 2% Yb composition and slowly decreases as more $\mathrm{Yb}_\mathrm{Pb}^{1+}$ and compensating $\mathrm{V}_\mathrm{Pb}^{2-}$ are added to the system. Consequently, for higher Yb incorporation, we witness, on average, a growth in the 1NN $\mathrm{Yb}_\mathrm{Pb}^{1+}$-coordination number z around each $\mathrm{V}_\mathrm{Pb}^{2-}$. In particular, we find that the addition of a third $\mathrm{Yb}_\mathrm{Pb}^{1+}$ in the coordination environment around a Pb vacancy costs very little additional energy (<0.05 eV), which we subsequently verified by DFT. Thus, the observed increase in the proportion of $z = 3$ defect motifs is essentially the result of the random placement of additional Yb on an increasingly occupied Pb sublattice. Nonetheless, we find that $(2\mathrm{Yb_{Pb}} + \mathrm{V_{Pb}})^0$ and their partially dissociated counterparts $(\mathrm{Yb_{Pb}} + \mathrm{V_{Pb}})^{1-}$ remain the dominant complex motifs over the range of compositions considered here. Indeed, consistent with the findings of Roh *et al.*, under similar conditions (single-crystal samples with 2% Yb fraction) [12], we find that multiple, distinct $\mathrm{Yb_{Pb}}$-$\mathrm{V_{Pb}}$ complex configurations are present in significant quantities at room temperature. Roh *et al.* further suggested that a specific Yb defect motif accounts for the majority of quantum-cutting PL intensity [12]. Fully delineating, based on first principles, the extent to which different local Yb configurations relative to a Pb vacancy influence local energy transfer is beyond the scope of this work, although we comment further on this in Sec. II D. However, we do find that among the distinct $(2\mathrm{Yb_{Pb}} + \mathrm{V_{Pb}})^0$ complexes present in the simulation, the OT configurations are roughly three times more prevalent than the CL configurations [Fig. 7(b)].

Of particular relevance to the proposed Yb-mediated quantum cutting mechanism is the probability that pairs of Yb substitutionals can be found within a critical distance of each other. We take this cutoff to be the distance ($\approx$12 Å) between third-nearest-neighbor (3NN) sites on the Pb sublattice, which corresponds to the maximal span of the CL configuration of the neutral $(2\mathrm{Yb_{Pb}} + \mathrm{V_{Pb}})^0$ complex and is of the order of the estimated exciton Bohr radius (see Sec. II D and Table III). In Fig. 7(c), we plot the fraction of $\mathrm{Yb}_\mathrm{Pb}^{1+}$ in the system surrounded by w additional $\mathrm{Yb}_\mathrm{Pb}^{1+}$ within this 3NN shell, as predicted by our room-temperature MC simulations. Again, for very dilute Yb compositions, $\mathrm{Yb}_\mathrm{Pb}^{1+}$ are predominantly isolated, but long-range Coulomb interactions quickly lead to bound $\mathrm{Yb_{Pb}}$-$\mathrm{V_{Pb}}$ complexes as the Yb composition increases. As the Yb composition approaches 10%, the average contact distance between $\mathrm{Yb}_\mathrm{Pb}^{1+}$ pairs decreases monotonically. In particular, we find that above 1% Yb, the majority of $\mathrm{Yb}_\mathrm{Pb}^{1+}$ are within 12 Å of at least one other $\mathrm{Yb}_\mathrm{Pb}^{1+}$. This is consistent with the observed onset of significant NIR PLQY in Yb:$\mathrm{CsPbCl_3}$ [3,4]. Moreover, in modeling the PL kinetics of Yb-doped $\mathrm{CsPb(Cl_{1-x}Br_x)_3}$, Erickson *et al.* found that an effective quantum-cutting rate proportional to the number of Yb dimers in a specific pairing better reproduced the experimentally observed Yb-concentration dependence in the PLQY compared to a rate proportional to all possible pairs of Yb [32]. This supports the hypothesis that the propensity for pairs of Yb to participate in quantum cutting depends on their relative spatial arrangement [32]. Implicit in their argument was the locality of these Yb dimers, although they did not model it explicitly. Furthermore, they experimentally verified that increasing the Yb concentration provided an effective route toward reducing PL saturation at higher photoexcitation rates by increasing the relative fraction of singly excited Yb dimers in the steady state [32]. For small, but increasing Yb incorporation, we find that the fraction of local configurations with at least two $\mathrm{Yb}_\mathrm{Pb}^{1+}$ at 1NN positions around a Pb vacancy grows more rapidly than at higher Yb incorporation [Fig. 7(a)]. This initial nonlinear behavior is due not only to the low probability of finding local Yb pairs for very dilute Yb concentrations, but also depends on the initial scarcity of compensating $\mathrm{V}_\mathrm{Pb}^{2-}$. This may provide some explanation for the observed disappearance of excitonic PL in NCs, noted by Milstein *et al.*, as a function of Yb doping, although competing exciton recombination processes may eliminate this behavior in SCs [3,12]. Further increasing the Yb fractions leads to the majority of Pb vacancies being coordinate by two or more $\mathrm{Yb}_\mathrm{Pb}^{1+}$. Importantly, the growth in local configurations with $z \geqslant 2$ is monotonic and weakly nonlinear beyond 2% Yb incorporation, which is consistent with the mechanism proposed by Erickson *et al.* for reducing PL saturation by increasing Yb concentration [32].

D. Exciton binding and defect localization

The quantum-cutting mechanism proposed by Milstein *et al.* relies not only on the spatial proximity of two $\mathrm{Yb}_\mathrm{Pb}^{1+}$ to a Pb vacancy, but also on the capacity for this doping-induced defect state to bind a photogenerated exciton [3,4,12]. In this picture, the Pb vacancy is thought to play the primary role in the initial energy capture before subsequent energy transfer to the nearby $\mathrm{Yb}_\mathrm{Pb}^{1+}$ pair. The shallow nature of this defect state is

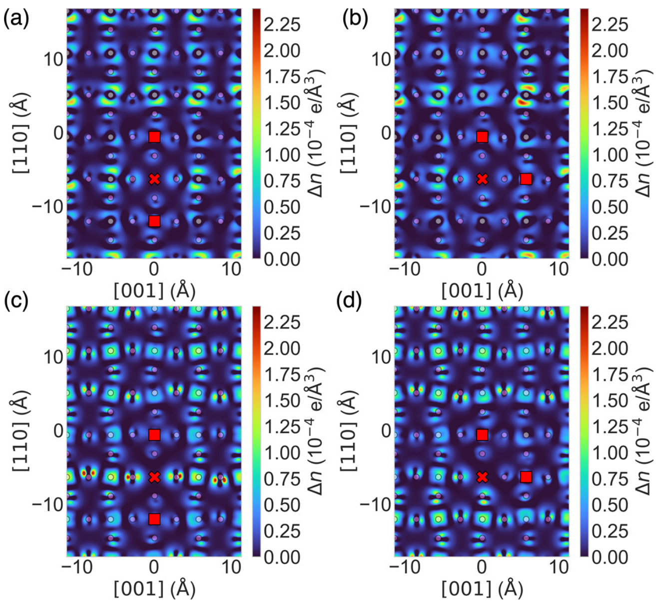

FIG. 8. Electron density differences for 2Yb$_{\mathrm{Pb}}$ + V$_{\mathrm{Pb}}$ complex in the (a),(c) CL [110] and (b),(d) OT $[110]^{\perp}$ configurations. (a),(b) The difference in electron density between the (−1) and neutral charge states associated with the $(0|-1)$ charge transition; (c),(d) the difference between the neutral and (+1) charge states associated with the $(1|0)$ charge transition. Density differences are displayed in the plane spanned by the defect complex, where the locations of the Yb$_{\mathrm{Pb}}$ (red squares) and V$_{\mathrm{Pb}}$ (red crosses) are indicated. The locations of nominal Pb (gray dots) and Cl (purple dots) sites in the undistorted, cubic perovskite phase are also provided for spatial reference.

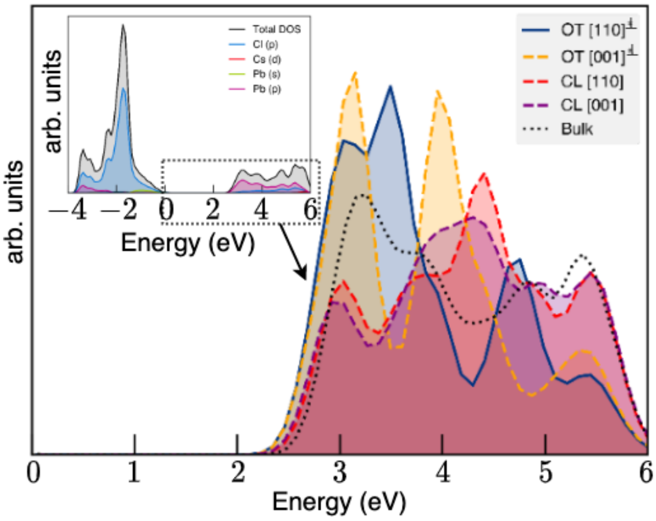

FIG. 9. Projected density of states near the conduction band edge for p orbitals of Pb sites equidistant from both Yb$_{\mathrm{Pb}}$ in $(2\mathrm{Yb}_{\mathrm{Pb}} + \mathrm{V}_{\mathrm{Pb}})^0$ defect supercells. (Inset: Total and projected density of states for bulk CsPbCl$_3$.)

particularly important, as it facilitates energy localization on the picosecond timescale and is unlikely to decrease the exciton Bohr radius beyond the scale required for simultaneous electronic coupling to both $\mathrm{Yb}_{\mathrm{Pb}}^{1+}$.

In Sec. II A, we noted the existence of $(1|0)$ and $(0|-1)$ transitions close to the VBM and CBM, respectively, for the $(2\mathrm{Yb}_{\mathrm{Pb}} + \mathrm{V}_{\mathrm{Pb}})^0$ complex. To assess the degree of charge carrier localization by the complex, Fig. 8 shows the difference in DFT electron densities in the plane spanned by the low-energy OT $[110]^{\perp}$ and CL [110] configurations for both the $(1|0)$ and $(0|-1)$ charge transitions. To emulate optical excitations, the relaxed atomic positions and lattice parameters from the neutral state are fixed in the (±1) charge states. A hole added to the valence band predominantly localizes on Cl and Pb sites, indicative of the fact that the top of the valence band of bulk CsPbCl$_3$ is primarily composed of Pb(s)-Cl(p) antibonding orbitals [13]. Furthermore, we find that the CL configuration shows marginally stronger charge localization on Cl sites closest to the Pb vacancy, while charge is more evenly distributed across the supercell for the OT configuration. Broadly speaking, the distribution of the added charge carrier reflects the symmetry of the defect configuration. This is particularly apparent in the electron density for the $(0|-1)$ charge transition, where the density distribution of an electron added to the conduction band among Pb p states (cf. Fig. 9) depends on the configuration of the complex. While the CL configuration shows several Pb sites in chains orthogonal to the complex with somewhat higher electron density, the reduced symmetry of the OT configuration leads to more localization on Pb sites closer to the Yb$_{\mathrm{Pb}}$. Nonetheless, the charge carrier remains relatively delocalized across the supercell, regardless of the defect configuration. Using Bader charge analysis, we have also verified that this charge delocalization persists after allowing for lattice relaxation in the (±1) charge states [43].

It is worth noting that similar differences in Pb-site electron density were reported by Li *et al.* in DFT calculations of OT $(2\mathrm{Yb}_{\mathrm{Pb}} + \mathrm{V}_{\mathrm{Pb}})^0$ defect complexes in cubic CsPbCl$_3$ [30]. Following their analysis, in Fig. 9 we plot the site- and orbital-projected density of states (pDOS) near the conduction band edge for the p states of Pb sites equidistant from both Yb$_{\mathrm{Pb}}$ in the neutral, fully bound defect motifs. Relative to bulk Pb sites, the OT configurations exhibit a higher intensity in the local pDOS near the band edge. The low-energy OT $[110]^{\perp}$ configuration, in particular, features a broader band of higher pDOS close to the CBM, which may be attributable to the lower Yb-site symmetry noted in Sec. II B. In contrast, the CL configurations show a decreased intensity in their local Pb-site pDOS near the conduction band edge relative to the bulk. This raises the prospect that excited electrons could have a higher probability to populate conduction band states at Pb sites closer to an OT complex [30]. The comparably lower probability associated with CL complexes could provide a mechanism through which only certain local defect complex configurations dominate quantum cutting. However, in accounting for electronic relaxation in calculating the DFT electron densities, Fig. 8 reveals a more complicated picture: Pb sites closer to the Yb$_{\mathrm{Pb}}$ show somewhat higher electron density, but only marginally so.

We find that the Yb$_{\mathrm{Pb}}$ appear to play a secondary role in determining how charge carriers redistribute in the system. Specifically, only a small fraction of charge added to the neutral system ends up on Yb sites or their immediate environment. Moreover, Bader charge analysis reveals that both Yb ions in the neutral complex, regardless of the configuration, have a nominal (+2) Bader valence [44] due to charge compensation by the Pb vacancy, and this valence state does not appreciably change upon adding a charge carrier (either electron or hole) to the supercell [43]. This is somewhat expected given the shallow nature of the complex and the constituent point defects (Fig. 2 and Table III), which primarily act as perturbations to the host band states.

Finite-size limits on the DFT supercell make it difficult to definitively resolve spatial features of delocalized charge carriers in shallow defect states in the thermodynamic limit [17]. Moreover, the above analysis is limited by the fact that standard Kohn-Sham DFT is fundamentally a theory of electronic ground states, rather than excited-state quasiparticles. Unfortunately, direct excited-state calculations of defects from first principles are often prohibitively computationally expensive. Given that the Pb vacancy acts as a doubly charged acceptor, while the $\mathrm{Yb}_{\mathrm{Pb}}$ are only singly charged, the Pb vacancy should provide the dominant contribution to the binding of an exciton. Thus, as an alternative route toward characterizing the role of the defect complex in localizing a photogenerated exciton, we consider an effective model of exciton binding to a $\mathrm{V}_{\mathrm{Pb}}^{2-}$, via the following three-body Hamiltonian in the Born-Oppenheimer adiabatic approximation:

$$\hat{H} = -\frac{1}{2}\nabla_1^2 - \frac{1}{2\sigma}\nabla_2^2 - \frac{q_d}{r_1} + \frac{q_d}{r_2} + V(r_{12}), \tag{18}$$

with energies $[m_e^* m_0 e^4/(\epsilon_0\epsilon_s\hbar)^2]$ and lengths $[\epsilon_0\epsilon_s\hbar^2/(m_e^* m_0 e^2)]$ rescaled to atomic units [45]. The ratio of hole and electron effective masses, $\sigma = m_h^*/m_e^*$, is a free parameter in the model. The relative distances of a conduction band electron and a valence band hole to the defect center with nominal charge state $q_d = -2$ are denoted r_1 and r_2, respectively, while the electron and hole effective masses $m_{e,h}^*$ were determined from the DFT band structure (cf. Appendix A). The static dielectric constant ϵ_s and the high-frequency, optical dielectric constant ϵ_∞ of the material were determined using density functional perturbation theory (Table III).

We have implicitly assumed that defect-charge carrier Coulomb interactions are screened by the static dielectric constant ϵ_s, while the electron-hole interaction $V(r_{12})$ is allowed to take a more general form [46]. In particular, the softness and ionic nature of the perovskite lattice and the large difference between the static and high-frequency dielectric constants implies strong Fröhlich coupling $\alpha_{e,h} = (e^2/\hbar\epsilon_*)\sqrt{m_{e,h}^*/2E_{\mathrm{LO}}}$ between charge carriers and longitudinal optical (LO) phonons, where $1/\epsilon_* = 1/\epsilon_\infty - 1/\epsilon_s$ and E_{LO} is a characteristic LO excitation energy (see below). The associated formation of large polarons has been previously invoked as a primary source of disagreement between measurements of the exciton binding energy in metal-halide perovskites [47–54]. To account for the possible relevance of polaron formation, we consider the effective polaron interaction potential derived by Haken (H),

$$V_{\mathrm{H}}(r) = -\frac{e^2}{\epsilon_s r} - \frac{e^2}{2\epsilon_* r}\left(e^{-r/l_h} + e^{-r/l_e}\right), \tag{19}$$

where electron- and hole-polaron radii are given by $l_{e,h} = \sqrt{\hbar^2/2m_{e,h}^* E_{\mathrm{LO}}}$, and the kinetic energy terms in the Hamiltonian (18) contain the renormalized effective masses $\tilde{m}_{e,h}^*$ [55–57],

$$\tilde{m}_{e,h}^* = m_{e,h}^*\left(1 + \frac{\alpha_{e,h}}{6}\right). \tag{20}$$

Previous studies have noted that the Haken model often overestimates the exciton binding energy in certain polar semiconductors and insulators [46,47,58]. Thus, we also consider the phenomenological model proposed by Pollmann and Büttner (PB),

$$V_{\mathrm{PB}}(r) = -\frac{e^2}{\epsilon_s r} - \frac{e^2}{\epsilon_* r}\left(\frac{m_h^*}{\Delta m^*}e^{-r/l_h} - \frac{m_e^*}{\Delta m^*}e^{-r/l_e}\right), \tag{21}$$

where $\Delta m^* = m_h^* - m_e^*$, and the bare electron and hole effective masses $m_{e,h}^*$ are used in the kinetic energy terms in the Hamiltonian (18) [59]. At short range, both models behave as a Coulomb potential with weaker screening by the optical dielectric constant ϵ_∞, while at long range, the interaction is strongly screened by the static dielectric constant ϵ_s. From a strictly mathematical point of view, the Pollmann-Büttner model has the advantage of interpolating between the extreme cases of $\lim_{l_{e,h}\to 0} V(r_{12}) \propto 1/\epsilon_s r_{12}$ and $\lim_{l_{e,h}\to\infty} V(r_{12}) \propto 1/\epsilon_\infty r_{12}$, depending on the length scales $l_{e,h}$.

We take a variational approach to approximating the ground state of the effective Hamiltonian (18) using a wavefunction ansatz $|\Psi\rangle$ expanded in the following s-wave basis $|\psi_i\rangle$:

$$|\Psi\rangle = \sum_i c_i|\psi_i\rangle, \tag{22}$$

$$|\psi_i\rangle = \exp\left(-\alpha_i r_1 - \beta_i r_2 - \gamma_i r_{12}\right). \tag{23}$$

Prior works have shown that this class of exponentially correlated variational ansatz can yield highly accurate ground-state predictions on few-body quantum systems with a relatively small number of basis functions [46,61–64]. The variational parameters $(\alpha_i, \beta_i, \gamma_i, c_i)$ were optimized according to a two-step procedure discussed in Appendix B.

The binding energy E_X for a Wannier-Mott exciton in CsPbCl_3 provides a natural reference point for the variational ground-state energy E_{GS} of the defect-bound exciton. We use a standard hydrogenic model to obtain a baseline estimate for E_X, along with the effective exciton Bohr radius a_{B}^*,

$$E_X = \frac{m_r}{m_0}\left(\frac{\epsilon_0}{\epsilon_r}\right)^2 E_{\mathrm{Ry}}, \tag{24}$$

$$a_{\mathrm{B}}^* = \frac{m_0}{m_r}\left(\frac{\epsilon_r}{\epsilon_0}\right) a_{\mathrm{B}}, \tag{25}$$

where the reduced mass of the exciton is $m_r = (1/m_e^* + 1/m_h^*)^{-1}$, and we take the relative dielectric constant ϵ_r to be equal to the high-frequency dielectric constant ϵ_∞ (Table III) [66]. With this choice of dielectric constant along with the effective masses from DFT, we predict an exciton binding energy of ≈72 meV, which agrees well with the experimental values of 72 ± 3 meV reported by Zhang *et al.* [67] and 64 ± 1.5 meV reported by Baranowski *et al.* in CsPbCl_3 [65,68,69]. The associated exciton Bohr radius (2.46 nm) is used in the analysis of Sec. II C.

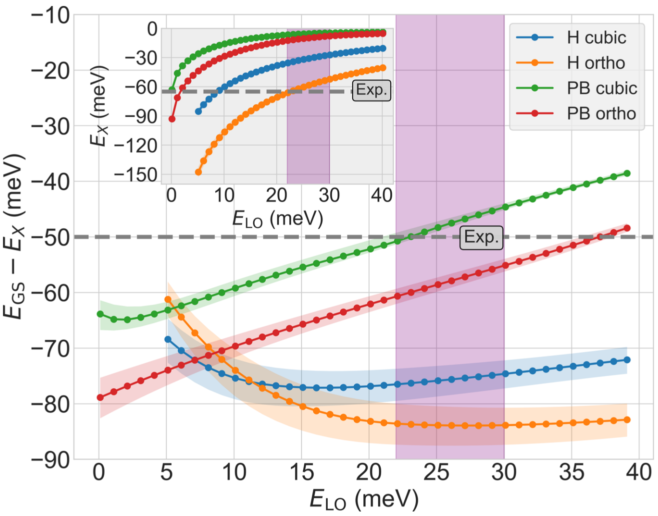

FIG. 10. Variational ground-state energy E_{GS} of a polaronic exciton bound to double acceptor A^{2-} with respect to polaronic exciton binding energy E_X (inset) as a function of characteristic phonon energy E_{LO}. Polaronic effects are incorporated either by the Haken (H) model or the Pollmann-Büttner (PB) model for both the cubic and orthorhombic perovskite phases, with additional uncertainty in the effective mass ratio included. The shaded, vertical region highlights the predicted range of E_{LO} from first-principles calculations for CsPbCl$_3$. Current experimental values for $E_{\mathrm{GS}} - E_X$ from shallow trap emission and for E_X from magneto-optical response (gray, dashed lines) are also included [3,65].

To provide a consistent point of comparison to the variational ground state of the Hamiltonian (18) including polaronic effects, we also consider the more general calculation of the exciton binding energy given by the Hamiltonian

$$\hat{H}_X = -\tfrac{1}{2}\nabla^2 + V(r), \tag{26}$$

where the electron-hole interaction potential is again taken to be either the Haken (19) or Pollmann-Büttner (21) model. The atomic units in the Hamiltonian (26) are set by the reduced exciton mass m_r, determined either by the renormalized polaron masses (20) for the Haken potential or the bare effective masses for the Pollmann-Büttner potential. We use the following variational ansatz:

$$|\Psi_X\rangle = \frac{\gamma^{3/2}}{\sqrt{\pi}} e^{-\gamma r}, \tag{27}$$

to obtain the exciton binding energy $E_X \approx \min_\gamma \langle \Psi_X | \hat{H}_X | \Psi_X \rangle$.

In Fig. 10, we compare the difference between the ground-state energy of an exciton bound to a double acceptor E_{GS} and the exciton binding energy E_X described by either the Haken (19) or Pollmann-Büttner (21) models and for various choices of physical model parameters. Since the effective masses and static dielectric constant are sensitive to the structure of the CsPbCl$_3$ lattice (Table III), we consider both sets of parameters determined by DFT for the high-temperature cubic $Pm\bar{3}m$ phase and the low-temperature orthorhombic $Pnma$ phase. Furthermore, since the effective band masses derived from DFT may vary based on the choice of semilocal or hybrid functionals and spin-orbit coupling, we allow for an uncertainty of ±0.05 in the ratio $\sigma = m_h^*/m_e^*$ of effective masses commensurate with variations reported in the literature [50,52,70]. In Fig. 10, we treat the effective LO phonon energy E_{LO} as a free parameter. This is done not only to exhibit the dependence of $E_{\mathrm{GS}} - E_X$ on the LO phonon spectra, but also to show the limit $l_{e,h} \to \infty$ of the Pollmann-Büttner model, tantamount to an electron-hole Coulomb interaction weakly screened by the optical dielectric constant ϵ_∞. Of course, this limit is unphysical from the standpoint of the underlying continuum polaron theory [71], which assumes weak to intermediate Fröhlich couplings $\alpha_{e,h} < 6$, but it provides a useful lower bound on the defect-bound exciton ground state as a function of the choice of electron-hole interaction model [55–57,59]. Specifically, in terms of formulating the effective Hamiltonian (18), this limit corresponds to short-timescale electron-hole interactions against an effectively frozen lattice. We estimate the LO phonon energy $E_{\mathrm{LO}} = \hbar\tilde{\omega}_{\mathrm{LO}} \approx 26$ meV by taking the LO frequency $\tilde{\omega}_{\mathrm{LO}}$ to be the location of the peak of the loss function $\mathrm{Im}[-\epsilon(\omega)^{-1}]$ in the midinfrared [50,51,72]. This is close to the values ≈26.5 ± 1.5 meV found by Carabatos-Nédelec *et al.* for CsPbCl$_3$ [73] and ≈28 meV found by Sender *et al.* for CH$_3$NH$_3$PbCl$_3$ [50]. This apparent independence to the identity of the A-site cation is to be expected since LO phonons in ABX_3 halide perovskites within this frequency range correspond to Pb-X stretching modes [50,51,74]. In the orthorhombic $Pnma$ phase, this predicted value of E_{LO} corresponds to dimensionless Fröhlich coupling constants $\alpha_e = 2.37$ and $\alpha_h = 2.30$, while the renormalized, reduced exciton-polaron mass, $\tilde{m}_r = 0.18$, compares well with value of 0.20 ± 0.01 reported by Baranowski *et al.* [65]. The region of the predicted LO phonon energy E_{LO}, allowing for uncertainty of the order of the optical phonon bandwidth, is included in Fig. 10.

Milstein *et al.* have reported shallow trap emission at ≈50 meV below the excitonic PL associated with a RE^{3+} dopant-induced defect state [3]. We find that the Pollmann-Büttner model parameterized by the effective masses and dielectric constants in the cubic $Pm\bar{3}m$ phase predicts $E_{\mathrm{GS}} - E_X$ to be within 10 meV of this experimental value for most values of the effective LO phonon energy, with particularly good agreement within the *ab initio* range of E_{LO}. When using the heavier effective masses for the orthorhombic $Pnma$ phase, the exciton is more tightly bound to the defect by an energy difference ≈10 meV lower than the cubic phase. However, for both parameter sets, the Pollmann-Büttner model predicts a very weak exciton binding energy $E_X \approx 5$–15 meV for the *ab initio* range of E_{LO} (inset to Fig. 10) compared to the reported experimental values [65,67–69].

The Haken model, with parameters set to the orthorhombic phase, shows better agreement to the reported experimental exciton binding energies in this range. Menéndez-Proupin *et al.*, after correcting a problem in their calculation, made a similar observation that the Haken model better predicted the experimental exciton binding energy in CH$_3$NH$_3$PbI$_3$ [48,49]. Nonetheless, we find that the Haken model, as expected, predicts a stronger defect localization energy with $E_{\mathrm{GS}} - E_X$ of the order of 80 meV. Finally, the case where $V(r_{12}) \propto 1/\epsilon_\infty r_{12}$ in the Hamiltonian (18) and Wannier-Mott exciton binding (24) shows decent agreement to both the doping-induced defect state PL and the experimental exciton binding energy for the cubic phase, while stronger binding is again found for the orthorhombic phase (Table III). In this case, we also calculate the expectation value of the radius $\langle r_{12} \rangle$ for the defect-bound exciton (Table III), verifying for both the cubic and orthorhombic phases that while the spatial extent of the exciton is reduced, it remains sufficiently delocalized to simultaneously couple to both $\mathrm{Yb}_{\mathrm{Pb}}^{1+}$ in a local configuration of the fully compensated complex. As this model possesses the lowest degree of screening among those considered, it provides a characterization of the exciton length scale in the maximally localized case.

In light of the above discussion, let us make some additional comments on interpreting these results. First, to simplify the variational problem defined by (18), we have neglected the role of the $\mathrm{Yb}_{\mathrm{Pb}}^{1+}$ pair in exciton localization. It is reasonable to expect, based on electrostatics, that the addition of $\mathrm{Yb}_{\mathrm{Pb}}^{1+}$ will increase the defect-bound exciton ground-state energy and that the OT configuration of the fully compensated complex should have marginally stronger binding relative to the CL configuration. Thus, our model predictions should provide an approximate lower bound on the ground-state energy of the exciton bound to the full defect complex, and this is generally what we find in comparing to the shallow trap emission reported by Milstein *et al.* [3].

Whether polaronic effects are fundamental to the interpretation of the experimental data remains somewhat of an open question. We found, for instance, that a simple Coulombic electron-hole interaction screened by the optical dielectric constant seems to account for the essential contributions to both the experimental localization energy and the exciton binding energy. However, justification of this model relies on an accurate assessment of the relevant timescales involved in the experimental technique and the exciton lifetime. At very short times ($\lesssim$200 fs), the exciton should only be subject to screening by electronic degrees of freedom, while screening by lattice polarization becomes relevant at longer times [49,65,70,75–77]. Indeed, Miyata *et al.* found that large polaron formation occurred on a timescale of 0.7 ps in $\mathrm{CsPbBr_3}$ [51]. In contrast, energy transfer from the exciton to the RE^{3+} dopant-induced defect state occurs on a timescale of a few picoseconds, while energy transfer to the Yb pair occurs of the order of a few nanoseconds, suggesting that ionic contributions to the dielectric screening should be considered [3,4,12].

It has been argued that transmission measurements based on a high-field magneto-optical response, for which the high cyclotron frequency is expected to decouple charge carrier motion from lattice polarization, can lead to overestimations of the experimental exciton binding energy by factors of 3–4 for methylammonium lead halide perovskites $\mathrm{CH_3NH_3Pb}X_3$ [75,77–79]. Similar behavior can be expected for the class of inorganic lead halide perovskites $\mathrm{CsPb}X_3$, as the electronic structure and dielectric screening are largely determined by the $[\mathrm{Pb}X_3]^{1-}$ sublattice [51,80]. However, the magneto-optical measurements of the exciton binding energy reported by Baranowski *et al.* [65] should be robust against this error since the authors explicitly extrapolate to the zero-field limit, following the earlier studies [78,80]. Their reported values are further substantiated by the similar values obtained by Zhang *et al.* [67] using absorption spectroscopy.

Recent theoretical work by Filip *et al.* [60] found that LO phonon screening could account for a significant fraction of the discrepancy between experimental exciton binding energies in orthorhombic $\mathrm{CsPb}X_3$ and the overestimated values predicted by the *ab initio* Bethe-Salpeter equation (BSE), which traditionally included only electronic screening effects [53,54]. Moreover, they established that an isotropic, parabolic band approximation was sufficient to capture the lowest-order phonon screening contribution ΔE_X to the BSE exciton binding energy due to Frölich-type electron-phonon interactions, leading to the analytic expression

$$\Delta E_X = -2E_{\mathrm{LO}}\left(1-\frac{\epsilon_\infty}{\epsilon_s}\right)\frac{3+\sqrt{1+\frac{E_{\mathrm{LO}}}{E_X}}}{\left(1+\sqrt{1+\frac{E_{\mathrm{LO}}}{E_X}}\right)^3}. \qquad (28)$$

By ignoring the electronic band dispersion entirely [60], this correction further simplifies to

$$\Delta E_X = -2\left(1-\frac{\epsilon_\infty}{\epsilon_s}\right)\frac{E_X E_{\mathrm{LO}}}{E_X+E_{\mathrm{LO}}}. \qquad (29)$$

For the *Pnma* phase (Table III), we find that the correction (28) brings the Wannier-Mott value (24) for the exciton binding energy to within 10 meV of the value reported by Zhang *et al.* [67]. Furthermore, it is interesting to note that the dispersionless correction (29) yields close agreement to the exciton binding energy predicted by the Haken model ($E_X^{(\mathrm{H})} \approx 58$ meV). This correction (29) is also commensurate with the shift in E_{GS} predicted by the Haken model relative to the electronically screened $V(r_{12}) \propto 1/\epsilon_\infty r_{12}$ model in (18). Thus, it is entirely plausible that phonon screening provides a significant contribution to the defect-bound exciton ground state, as well as to the stability of the free exciton. While we find that there is relatively little difference between the Haken model prediction of $E_{\mathrm{GS}} - E_X$ compared to the electronically screened model, a lower exciton binding energy would imply a higher rate of thermal dissociation and could entail greater competition from alternative pathways for carrier recombination. This may be reasonable given that Roh *et al.* did not observe excitonic PL in their SC sample over a broad range of temperatures and suggests that upstream energy losses are reduced in NCs, which exhibited higher PLQYs [12]. Finally, our finding that charge compensation increases the total concentration of $\mathrm{V}_{\mathrm{Pb}}^{2-}$ with increasing Yb incorporation (Sec. II C) would then explain why Milstein *et al.* do not observe shallow trap emission without RE^{3+} doping [3].

III. CONCLUSIONS

The fortuitous energy matching between the band gap of $\mathrm{CsPb(Cl}_{1-x}\mathrm{Br}_x)_3$ and f-f transitions in Yb enables the surprisingly efficient sensitization of Yb luminescence via quantum cutting [35]. A steady accumulation of experimental evidence points to the role played by $(2\mathrm{Yb_{Pb}} + \mathrm{V_{Pb}})^0$ defect complexes in facilitating these quantum-cutting processes, where a shallow doping-induced defect state localizes a photogenerated charge carrier and the spatial proximity of pairs of Yb allows for simultaneous energy splitting and NIR emission of pairs of photons [3,4,12,32–35]. However, atomistic details of the defect structure, its expected concentration, and its coupling to the surrounding perovskite material have remained largely undetermined. To that end, we have attempted to resolve some of these details using density functional theory and various effective models for defect formation and charge carrier localization. We found, for instance, that $\mathrm{Yb_{Pb}}$-$\mathrm{V_{Pb}}$ complexes and their constituent point defects introduce only shallow defect levels into the electronic structure of the material. While Cl vacancies form deeper amphoteric defect states, their predicted concentration is limited under the experimentally relevant Cs-rich, moderately Pb-poor synthesis conditions. Increasing Yb incorporation under these conditions was also found to increase the concentration of Pb vacancies and $\mathrm{Yb_{Pb}}$-$\mathrm{V_{Pb}}$ complexes via charge compensation. Together, these results are consistent with the hypothesis that high PLQYs in Yb:$\mathrm{CsPbCl_3}$ are driven by $(2\mathrm{Yb_{Pb}} + \mathrm{V_{Pb}})^0$ defect-mediated quantum cutting [3].

We observed that various configurations of the $(2\mathrm{Yb_{Pb}} + \mathrm{V_{Pb}})^0$ defect complex possess favorable binding energy, where orthogonal motifs are marginally more stable than collinear ones. Screened electrostatic interactions account for most of the complex binding energy, while patterns of local bonding and induced strain provide additional contributions to the small energetic differences between local motifs. We have further characterized, on the basis of a self-consistent thermodynamic model of defect concentrations, how both charge and strain compensation between $\mathrm{V_{Pb}^{2-}}$ and $\mathrm{Yb_{Pb}^{1+}}$ limits the change in lattice volume under Yb doping, which may account for the lack of appreciable shifts in the XRD data between undoped and Yb-doped $\mathrm{CsPbCl_3}$ [3,4,12,33–35]. Using this thermodynamic model and Monte Carlo sampling, we approximated the room-temperature spatial distribution of $\mathrm{Yb_{Pb}^{1+}}$ relative to Pb vacancies as a function of material composition. We found, in particular, that the fraction of Pb vacancies locally coordinated by at least two $\mathrm{Yb_{Pb}^{1+}}$ grows monotonically with either increasing Yb incorporation or increasing Cs:Pb composition. Furthermore, $(2\mathrm{Yb_{Pb}} + \mathrm{V_{Pb}})^0$ and their partially dissociated counterparts, $(\mathrm{Yb_{Pb}} + \mathrm{V_{Pb}})^{1-}$, remain the dominant complex motifs over experimentally relevant compositions.

Finally, we noted that orthogonal $(2\mathrm{Yb_{Pb}} + \mathrm{V_{Pb}})^0$ defect motifs, compared to collinear motifs, showed marginally stronger Pb-site localization of the DFT electron density associated with the $(0|-1)$ charge transition level. Conversely, collinear motifs exhibited marginally stronger charge localization on Cl sites near the Pb vacancy for the $(1|0)$ transition, which fills a valence band hole. Nonetheless, charge remained essentially delocalized in these supercell calculations and, given the potential relevance of phonon screening and large polaron formation, we resorted to an effective few-body Hamiltonian to scrutinize the role of Pb vacancies in localizing photogenerated charge carriers in the system. Variational ground-state calculations predicted shallow defect-bound exciton states with energies lower than the free exciton binding energy, in qualitative agreement with the experimentally observed $\mathrm{RE^{3+}}$ dopant-induced shallow trap emission [3,4,12]. However, we found notable quantitative disagreements between choices of effective electron-hole interaction with electronic structure parameters determined from DFT. While the inclusion of polaronic effects via the Haken model predicts relatively strong binding to shallow, double-acceptor states, it also provides, among the considered models, the best approximation to the experimental exciton binding energy in the low-temperature *Pnma* phase. Reconciling the predicted localization energy of the defect-bound exciton with the value measured from $\mathrm{RE^{3+}}$ dopant-induced shallow trap emission likely requires a full treatment of the entire $2\mathrm{Yb_{Pb}} + \mathrm{V_{Pb}}$ defect complex.

ACKNOWLEDGMENTS

This research was supported through the UW Molecular Engineering Materials Center, a Materials Research Science and Engineering Center (Grant No. DMR-1719797) and was facilitated through the use of advanced computational, storage, and networking infrastructure provided by the Hyak supercomputer system and funded by the STF at the University of Washington. The authors thank Joo Yeon D. Roh, Tyler J. Milstein, and Kyle T. Kluherz for useful discussions.

APPENDIX A: FIRST-PRINCIPLES COMPUTATIONS

All first-principles calculations in this work were carried out using the Vienna Ab-Initio Simulation Package (VASP) [16,81]. Plane-wave, Kohn-Sham density functional theory calculations employed the all-electron projector-augmented wave (PAW) method in the generalized gradient approximation (GGA) with the semilocal PBEsol functional [15,82,83]. In the pseudopotentials, 9 electrons of Cs $(5s^2 5p^6 6s^1)$, 4 electrons of Pb $(6ws^2 6p^2)$, and 7 electrons of Cl $(3s^2 3p^5)$ were treated as valence electrons, while 13 f-state electrons in the $[\mathrm{Xe}]4f^{14}6s^2$ valence configuration of Yb were treated as frozen core states. Blocked Davidson iteration was used to optimize the electronic degrees of freedom. A plane-wave basis cutoff was set to 400 eV, and a Γ-centered k-point mesh was used for Brillouin-zone integration [84]. Only the Γ point was included in the 360-site defect supercell calculations ($3 \times 3 \times 2$ supercells of the 20-atom *Pnma* unit cell), while a $4 \times 4 \times 2$ k-point mesh was used for *Pnma* unit cell calculations. The conjugate gradient algorithm was used for structural optimization, and the volume, shape, and atomic positions were relaxed until interatomic Hellmann-Feynman forces were less than 0.01 eV/Å. Because Hellmann-Feynman forces are derived from the occupied valence states of the system and Pb p states primarily contribute to the conduction band, we ignored spin-orbit coupling in relaxing atomic structures. However, spin-orbit coupling was included in deriving bulk effective masses and dielectric constants. For defect formation energies and charge transition levels, we included postprocessing corrections for spurious electrostatic interactions following the scheme (FNV) proposed by Freysoldt, Neugebauer, and Van de Walle [18]. No additional corrections related to the GGA band gap or the absence of spin-orbit coupling were included. Molecular dynamics (MD) trajectories were calculated with VASP using the Nosé-Hoover thermostat and NVT ensemble for 100 time steps (2 fs each) at a temperature of 300 K. PDFs were generated by convolving the distribution of pairwise distances with a Gaussian distribution with standard deviation of 0.5 Å and averaging over the MD trajectories.

We note that the use of semilocal functionals such as PBEsol can often lead to predicted ground-state electron densities that are underlocalized, while an improved description

TABLE IV. Thermodynamic charge transition levels relative to the band edges predicted by PBEsol and HSE06. For reference, the PBEsol band gap is $E_{\text{gap}}^{(\text{PBE})} = 2.46$ eV, while the HSE06 band gap is $E_{\text{gap}}^{(\text{HSE})} = 3.27$ eV.

Defect $(q_1\|q_2)$	PBESol	HSE06
$2\text{Yb}_{\text{Pb}} + \text{V}_{\text{Pb}}$ $(0\|-1)$	$E_{\text{CBM}} - 0.003$	$E_{\text{CBM}} - 0.002$
Yb_{Pb} $(1\|0)$	$E_{\text{CBM}} - 0.057$	$E_{\text{CBM}} - 0.048$
V_{Pb} $(-1\|-2)$	$E_{\text{VBM}} + 0.158$	$E_{\text{VBM}} + 0.113$

of electronic structure can be obtained by mixing in some degree of Hartree-Fock exchange at the expense of a much more computationally demanding calculation [17]. We tested the consistency of our choice of functional for the primary defects studied in this work by comparing the charge transition levels (3) predicted by PBEsol to those predicted by the hybrid Heyd-Scuseria-Ernzerhof (HSE06) functional [85]. To reduce computational costs, we studied $2 \times 2 \times 1$ supercells of the *Pnma* unit cell with a $2 \times 2 \times 2$ k-point mesh. Table IV summarizes the charge transition levels for Yb_{Pb}, V_{Pb}, and the $2\text{Yb}_{\text{Pb}} + \text{V}_{\text{Pb}}$ complex in the OT $[001]^{\perp}$ configuration (see main text) predicted by PBEsol and HSE06, and measured relative to the respective band edges. We find that both the semilocal and hybrid functionals predict shallow defect states in all three cases and that the locations with respect to the band edges agree within the expected accuracy of these methods. This is consistent with our findings in larger supercells presented in the main text. Furthermore, in moving to HSE06, we did not observe increased localization in the electron density for the $2\text{Yb}_{\text{Pb}} + \text{V}_{\text{Pb}}$ complex.

Corrections to defect formation energies were computed with the help of the PYCDT and PYMATGEN programs with suitable modifications [86,87]. Bulk effective masses were derived from the computed band structures of the cubic $Pm\bar{3}m$ and the orthorhombic *Pnma* perovskite phases of CsPbCl_3 in the parabolic band approximation using weighted least-squares fitting as implemented in the EFFMASS program [88]. Additional normal mode and phonon spectra analysis utilized the PHONOPY program [89]. Visualizations of atomic structures were generated using the VESTA program [90].

APPENDIX B: VARIATIONAL CALCULATIONS OF DEFECT-BOUND EXCITONS

Variational ground states to the effective Hamiltonian (18) were determined according to the following procedure. The variational optimization problem with wave-function anzatz (22) can be formulated as a generalized eigenvalue problem,

$$H\mathbf{c} = ES\mathbf{c}, \tag{B1}$$

where $\mathbf{c}$ is the eigenvector of linear variational coefficients c_i in (22) associated with the minimal eigenvalue E. Hamiltonian matrix elements H and overlap integrals S,

$$H_{ij} = \langle \psi_i | \hat{H} | \psi_j \rangle, \tag{B2}$$

$$S_{ij} = \langle \psi_i | \psi_j \rangle, \tag{B3}$$

can be computed analytically for the class of exponentially correlated wave functions (23) by taking repeated derivatives of the fundamental Calais-Löwdin integral,

$$\Gamma_{0,0,0}(\alpha, \beta, \gamma) = \frac{2}{(\alpha + \beta)(\alpha + \gamma)(\beta + \gamma)}, \tag{B4}$$

with respect to the nonlinear variational coefficients (α, β, γ) [64,91]. An integral of the order of $l, m, n \geqslant 0$, defined as

$$\Gamma_{l,m,n}(\alpha, \beta, \gamma) = \frac{1}{8\pi^2} \int d\mathbf{r}_1 d\mathbf{r}_2 r_1^{l-1} r_2^{m-1} r_{12}^{n-1} e^{-\alpha r_1 - \beta r_2 - \gamma r_{12}}, \tag{B5}$$

is thus given by

$$\Gamma_{l,m,n}(\alpha, \beta, \gamma) = 2l!m!n! \sum_{l'=0}^{l} \sum_{m'=0}^{m} \sum_{n'=0}^{n} \frac{\binom{m-m'+l'}{l'} \binom{l-l'+n'}{n'} \binom{n-n'+m'}{m'}}{(\alpha + \beta)^{m-m'+l'+1} (\alpha + \gamma)^{l-l'+n'+1} (\alpha + \beta)^{n-n'+m'+1}}. \tag{B6}$$

The optimization of linear and nonlinear variational parameters were handled self-consistently by the repeated iteration of two fundamental steps. Initially, nonlinear variational parameters were chosen by quasirandom tempering within the finite intervals $\alpha_i^{(0)} \in [A_1, A_2]$, $\beta_i^{(0)} \in [B_1, B_2]$, and $\gamma_i^{(0)} \in [G_1, G_2]$,

$$\alpha_i^{(0)} = (A_2 - A_1)\left\{\tfrac{1}{2} i(i+1)\sqrt{p_1}\right\} + A_1, \tag{B7}$$

$$\beta_i^{(0)} = (B_2 - B_1)\left\{\tfrac{1}{2} i(i+1)\sqrt{p_2}\right\} + B_1, \tag{B8}$$

$$\gamma_i^{(0)} = (G_2 - G_1)\left\{\tfrac{1}{2} i(i+1)\sqrt{p_3}\right\} + G_1, \tag{B9}$$

where p_j are distinct prime numbers [46,63,92]. For a given set of nonlinear parameters, the linear coefficients c_i were then determined by solution to the generalized eigenvalue problem (B1). For a given solution c_i, the nonlinear parameters $(\alpha_i, \beta_i, \gamma_i)$ were subsequently refined using the multilevel single-linkage (MLSL) global optimization algorithm with a series of multistart local optimizations using the bound optimization by quadratic approximation (BOBYQA) algorithm, as implemented in the NLOPT package [93–96]. The finite bounds (A_i, B_i, G_i) on the nonlinear parameters were determined by finite grid search. Variational wave functions with up to 15 basis terms were found to give sufficiently converged results.

[1] G. Pan, X. Bai, D. Yang, X. Chen, P. Jing, S. Qu, L. Zhang, D. Zhou, J. Zhu, W. Xu, B. Dong, and H. Song, Doping lanthanide into perovskite nanocrystals: Highly improved and expanded optical properties, Nano Lett. **17**, 8005 (2017).

[2] D. Zhou, D. Liu, G. Pan, X. Chen, D. Li, W. Xu, X. Bai, and H. Song, Cerium and ytterbium codoped halide perovskite quantum dots: A novel and efficient downconverter for improving the performance of silicon solar cells, Adv. Mater. **29**, 1704149 (2017).

[3] T. J. Milstein, D. M. Kroupa, and D. R. Gamelin, Picosecond quantum cutting generates photoluminescence quantum yields over 100% in ytterbium-doped $CsPbCl_3$ nanocrystals, Nano Lett. **18**, 3792 (2018).

[4] D. M. Kroupa, J. Y. Roh, T. J. Milstein, S. E. Creutz, and D. R. Gamelin, Quantum-cutting ytterbium-doped $CsPb(Cl_{1-x}Br_x)_3$ perovskite thin films with photoluminescence quantum yields over 190%, ACS Energy Lett. **3**, 2390 (2018).

[5] P. Vergeer, T. J. H. Vlugt, M. H. F. Kox, M. I. den Hertog, J. P. J. M. van der Eerden, and A. Meijerink, Quantum cutting by cooperative energy transfer in $Yb_xY_{1-x}PO_4 : Tb^{3+}$, Phys. Rev. B **71**, 014119 (2005).

[6] D. Chen, Y. Wang, Y. Yu, P. Huang, and F. Weng, Near-infrared quantum cutting in transparent nanostructured glass ceramics, Opt. Lett. **33**, 1884 (2008).

[7] L. Xie, Y. Wang, and H. Zhang, Near-infrared quantum cutting in $YPO_4 : Yb^{3+}$, Tm^{3+} via cooperative energy transfer, Appl. Phys. Lett. **94**, 061905 (2009).

[8] B. M. van der Ende, L. Aarts, and A. Meijerink, Near-infrared quantum cutting for photovoltaics, Adv. Mater. **21**, 3073 (2009).

[9] J. J. Eilers, D. Biner, J. T. van Wijngaarden, K. Krämer, H.-U. Güdel, and A. Meijerink, Efficient visible to infrared quantum cutting through downconversion with the Er^{3+}-Yb^{3+} couple in $Cs_3Y_2Br_9$, Appl. Phys. Lett. **96**, 151106 (2010).

[10] J.-M. Meijer, L. Aarts, B. M. van der Ende, T. J. H. Vlugt, and A. Meijerink, Downconversion for solar cells in $YF_3 : Nd^{3+}$, Yb^{3+}, Phys. Rev. B **81**, 035107 (2010).

[11] H. Lin, D. Chen, Y. Yu, A. Yang, and Y. Wang, Near-infrared quantum cutting in Ho^{3+}/Yb^{3+} codoped nanostructured glass ceramic, Opt. Lett. **36**, 876 (2011).

[12] Joo Yeon D. Roh, M. D. Smith, M. J. Crane, D. Biner, T. J. Milstein, K. W. Krämer, and D. R. Gamelin, Yb^{3+} speciation and energy-transfer dynamics in quantum-cutting Yb^{3+}-doped $CsPbCl_3$ perovskite nanocrystals and single crystals, Phys. Rev. Materials **4**, 105405 (2020).

[13] H. Jin, E. Debroye, M. Keshavarz, I. G. Scheblykin, M. B. J. Roeffaers, J. Hofkens, and J. A. Steele, It's a trap! On the nature of localised states and charge trapping in lead halide perovskites, Mater. Horizons **7**, 397 (2019).

[14] M. R. Linaburg, E. T. McClure, J. D. Majher, and P. M. Woodward, $Cs_{1-x}Rb_xPbCl_3$ and $Cs_{1-x}Rb_xPbBr_3$ Solid Solutions: Understanding Octahedral Tilting in Lead Halide Perovskites, Chem. Mater. **29**, 3507 (2017).

[15] W. Kohn and L. J. Sham, Self-consistent equations including exchange and correlation effects, Phys. Rev. **140**, A1133 (1965).

[16] G. Kresse and J. Furthmüller, Efficient iterative schemes for *ab initio* total-energy calculations using a plane-wave basis set, Phys. Rev. B **54**, 11169 (1996).

[17] C. Freysoldt, B. Grabowski, T. Hickel, J. Neugebauer, G. Kresse, A. Janotti, and C. G. Van de Walle, First-principles calculations for point defects in solids, Rev. Mod. Phys. **86**, 253 (2014).

[18] C. Freysoldt, J. Neugebauer, and C. G. Vande Walle, Fully Ab Initio Finite-Size Corrections for Charged-Defect Supercell Calculations, Phys. Rev. Lett. **102**, 016402 (2009).

[19] J.-P. Ma, Y.-M. Chen, L.-M. Zhang, S.-Q. Guo, J.-D. Liu, H. Li, B.-J. Ye, Z.-Y. Li, Y. Zhou, B.-B. Zhang, O. M. Bakr, J.-Y. Zhang, and H.-T. Sun, Insights into the local structure of dopants, doping efficiency, and luminescence properties of lanthanide-doped $CsPbCl_3$ perovskite nanocrystals, J. Mater. Chem. C **7**, 3037 (2019).

[20] M. Zeng, F. Artizzu, J. Liu, S. Singh, F. Locardi, D. Mara, Z. Hens, and R. V. Deun, Boosting the Er^{3+} $1.5\,\mu m$ luminescence in $CsPbCl_3$ perovskite nanocrystals for photonic devices operating at telecommunication wavelengths, ACS Appl. Nano Mater. **3**, 4699 (2020).

[21] S. B. Zhang, The microscopic origin of the doping limits in semiconductors and wide-gap materials and recent developments in overcoming these limits: A review, J. Phys.: Condens. Matter **14**, R881 (2002).

[22] S. Lany and A. Zunger, Assessment of correction methods for the band-gap problem and for finite-size effects in supercell defect calculations: Case studies for ZnO and GaAs, Phys. Rev. B **78**, 235104 (2008).

[23] J. Kang and L.-W. Wang, High defect tolerance in lead halide perovskite $CsPbBr_3$, J. Phys. Chem. Lett. **8**, 489 (2017).

[24] From the thermodynamic charge transition levels, $\varepsilon(+1/0)$ and $\varepsilon(0/-1)$, the effective U parameters are approximately $U_{\text{eff}} = -0.41$ and -0.54 eV for $V_{Cl}^{(ap)}$ and $V_{Cl}^{(eq)}$, respectively.

[25] J. Coutinho, V. P. Markevich, and A. R. Peaker, Characterisation of negative-U defects in semiconductors, J. Phys.: Condens. Matter **32**, 323001 (2020).

[26] P. Yu and M. Cadona, *Fundamentals of Semiconductors* (Springer, Heidelberg, 2010).

[27] H. Shi and M.-H. Du, Shallow halogen vacancies in halide optoelectronic materials, Phys. Rev. B **90**, 174103 (2014).

[28] S. Lany and A. Zunger, Anion vacancies as a source of persistent photoconductivity in II-VI and chalcopyrite semiconductors, Phys. Rev. B **72**, 035215 (2005).

[29] S. Lany and A. Zunger, Light- and bias-induced metastabilities in $Cu(In,Ga)Se_2$ based solar cells caused by the $(V_{Se}$-$V_{Cu})$ vacancy complex, J. Appl. Phys. **100**, 113725 (2006).

[30] X. Li, S. Duan, H. Liu, G. Chen, Y. Luo, and H. Ågren, Mechanism for the extremely efficient sensitization of Yb^{3+} luminescence in $CsPbCl_3$ nanocrystals, J. Phys. Chem. Lett. **10**, 487 (2019).

[31] J. C. Thomas and A. Van der Ven, The exploration of nonlinear elasticity and its efficient parameterization for crystalline materials, J. Mech. Phys. Solids **107**, 76 (2017).

[32] C. S. Erickson, M. J. Crane, T. J. Milstein, and D. R. Gamelin, Photoluminescence Saturation in Quantum-Cutting Yb^{3+}-Doped $CsPb(Cl_{1-x}Br_x)_3$ Perovskite Nanocrystals: Implications for Solar Downconversion, J. Phys. Chem. C **123**, 12474 (2019).

[33] M. J. Crane, D. M. Kroupa, J. Y. Roh, R. T. Anderson, M. D. Smith, and D. R. Gamelin, Single-source vapor deposition of quantum-cutting $Yb^{3+} : CsPb(Cl_{1-x}Br_x)_3$ and other complex metal-halide perovskites, ACS Appl. Energy Mater. **2**, 4560 (2019).

[34] T. A. Cohen, T. J. Milstein, D. M. Kroupa, J. D. MacKenzie, C. K. Luscombe, and D. R. Gamelin, Quantum-cutting Yb^{3+}-doped perovskite nanocrystals for monolithic bilayer luminescent solar concentrators, J. Mater. Chem. A **7**, 9279 (2019).

[35] T. Milstein, K. Kluherz, D. Kroupa, C. S. Erickson, J. J. Yoreo, and D. R. Gamelin, Anion Exchange and the Quantum-Cutting Energy Threshold in Ytterbium-Doped $CsPb(Cl_{1-x}Br_x)_3$ Perovskite Nanocrystals, Nano Lett. **19**, 1931 (2019).

[36] A. Walsh, A. A. Sokol, and C. R. A. Catlow, Free energy of defect formation: Thermodynamics of anion Frenkel pairs in indium oxide, Phys. Rev. B **83**, 224105 (2011).

[37] E. Jedlicka, J. Wang, J. Mutch, Y.-K. Jung, P. Went, J. Mohammed, M. Ziffer, R. Giridharagopal, A. Walsh, J.-H. Chu, and D. S. Ginger, Bismuth doping alters structural phase transitions in methylammonium lead tribromide single crystals, J. Phys. Chem. Lett. **12**, 2749 (2021).

[38] J. S. Bechtel and A. Van der Ven, Octahedral tilting instabilities in inorganic halide perovskites, Phys. Rev. Materials **2**, 025401 (2018).

[39] J. Young and J. M. Rondinelli, Octahedral rotation preferences in perovskite iodides and bromides, J. Phys. Chem. Lett. **7**, 918 (2016).

[40] J.-P. Ma, J.-K. Chen, J. Yin, B.-B. Zhang, Q. Zhao, Y. Kuroiwa, C. Moriyoshi, L. Hu, O. M. Bakr, O. F. Mohammed, and H.-T. Sun, Doping induces structural phase transitions in all-inorganic lead halide perovskite nanocrystals, ACS Mater. Lett. **2**, 367 (2020).

[41] K. Watanabe, M. Koshimizu, T. Yanagida, Y. Fujimoto, and K. Asai, Luminescence and scintillation properties of La- and La,Ag-doped $CsPbCl_3$ single crystals, Jpn. J. Appl. Phys. **55**, 02BC20 (2016).

[42] D. L. Dexter, A theory of sensitized luminescence in solids, J. Chem. Phys. **21**, 836 (1953).

[43] G. Henkelman, A. Arnaldsson, and H. Jónsson, A fast and robust algorithm for Bader decomposition of charge density, Comput. Mater. Sci. **36**, 354 (2006).

[44] The Bader valence for a given lattice atom is defined here as the difference between the number of valence electrons in the isolated atom and the Bader (electron) charge within the atom-centered Bader volume.

[45] A. Szabo and N. S. Ostlund, *Modern Quantum Chemistry* (Dover, New York, 1996).

[46] V. H. Smith and P. Petelenz, Effective electron-hole interaction potentials and the binding energies of exciton-ionized-donor complexes, Phys. Rev. B **17**, 3253 (1978).

[47] M. Baranowski and P. Plochocka, Excitons in metal-halide perovskites, Adv. Energy Mater. **10**, 1903659 (2020).

[48] E. Menéndez-Proupin, C. L. B. Ríos, and P. Wahnón, Nonhydrogenic exciton spectrum in perovskite $CH_3NH_3PbI_3$, Phys. Status Solidi (RRL) **9**, 559 (2015).

[49] E. Menéndez-Proupin, C. L. B. Ríos, P. Wahnón, and R. Tempelaar, Erratum to: Nonhydrogenic exciton spectrum in perovskite $CH_3NH_3PbI_3$ [Phys. Stat. Solidi RRL **9**, 559 (2015)], Phys. Stat. Solidi (RRL) **13**, 1900075 (2019).

[50] M. Sendner, P. K. Nayak, D. A. Egger, S. Beck, C. Müller, B. Epding, W. Kowalsky, L. Kronik, H. J. Snaith, A. Pucci, and R. Lovrinčić, Optical phonons in methylammonium lead halide perovskites and implications for charge transport, Mater. Horiz. **3**, 613 (2016).

[51] K. Miyata, D. Meggiolaro, T. M. Trinh, P. P. Joshi, E. Mosconi, S. C. Jones, F. Angelis, and X.-Y. Zhu, Large polarons in lead halide perovskites, Sci. Adv. **3**, e1701217 (2017).

[52] M. Puppin, S. Polishchuk, N. Colonna, A. Crepaldi, D. N. Dirin, O. Nazarenko, R. De Gennaro, G. Gatti, S. Roth, T. Barillot, L. Poletto, R. P. Xian, L. Rettig, M. Wolf, R. Ernstorfer, M. V. Kovalenko, N. Marzari, M. Grioni, and M. Chergui, Evidence of Large Polarons in Photoemission Band Mapping of the Perovskite Semiconductor $CsPbBr_3$, Phys. Rev. Lett. **124**, 206402 (2020).

[53] M. Bokdam, T. Sander, A. Stroppa, S. Picozzi, D. D. Sarma, C. Franchini, and G. Kresse, Role of polar phonons in the photo excited state of metal halide perovskites, Sci. Rep. **6**, 28618 (2016).

[54] P. Umari, E. Mosconi, and F. D. Angelis, Infrared dielectric screening determines the low exciton binding energy of metal-halide perovskites, J. Phys. Chem. Lett. **9**, 620 (2018).

[55] H. Haken, On the quantum theory of the multi-electron system in the oscillating lattice. I, Z. Phys. **146**, 527 (1956).

[56] H. Haken, The theory of the exciton in the solid, Fortschr. Phys. **6**, 271 (1958).

[57] R. P. Feynman, Slow electrons in a polar crystal, Phys. Rev. **97**, 660 (1955).

[58] K. Bajaj, Effect of electron-phonon interaction on the binding energy of a Wannier exciton in a polarizable medium, Solid State Commun. **15**, 1221 (1974).

[59] J. Pollmann and H. Büttner, Effective Hamiltonians and bindings energies of Wannier excitons in polar semiconductors, Phys. Rev. B **16**, 4480 (1977).

[60] M. R. Filip, J. B. Haber, and J. B. Neaton, Phonon Screening of Excitons in Semiconductors: Halide Perovskites and Beyond, Phys. Rev. Lett. **127**, 067401 (2021).

[61] T. Skettrup, M. Suffczynski, and W. Gorzkowski, Properties of excitons bound to ionized donors, Phys. Rev. B **4**, 512 (1970).

[62] F. E. Harris and V. H. Smith, Highly compact wave functions for he-like systems, J. Phys. Chem. A **109**, 11413 (2005).

[63] A. J. Thakkar and V. H. Smith, Compact and accurate integral-transform wave functions. I. The $1S^1$ state of the helium-like ions from H^- through Mg^{10+}, Phys. Rev. A **15**, 1 (1977).

[64] F. E. Harris, A. M. Frolov, and V. H. Smith, Singular and non-singular three-body integrals for exponential wave functions, J. Chem. Phys. **121**, 6323 (2004).

[65] M. Baranowski, P. Plochocka, R. Su, L. Legrand, T. Barisien, F. Bernardot, Q. Xiong, C. Testelin, and M. Chamarro, Exciton binding energy and effective mass of $CsPbCl_3$: A magneto-optical study, Photon. Res. **8**, A50 (2020).

[66] L. Protesescu, S. Yakunin, M. I. Bodnarchuk, F. Krieg, R. Caputo, C. H. Hendon, R. Yang, A. Walsh, and M. V. Kovalenko, Nanocrystals of cesium lead halide perovskites ($CsPbX_3$, X = Cl, Br, and I): Novel optoelectronic materials showing bright emission with wide color gamut, Nano Lett. **15**, 3692 (2015).

[67] Q. Zhang, R. Su, X. Liu, J. Xing, T. C. Sum, and Q. Xiong, High-quality whispering-gallery-mode lasing from cesium lead halide perovskite nanoplatelets, Adv. Funct. Mater. **26**, 6238 (2016).

[68] D. Fröhlich, K. Heidrich, H. Künzel, G. Trendel, and J. Treusch, Cesium-trihalogen-plumbates a new class of ionic semiconductors, J. Lumin. **18-19**, 385 (1979).

[69] H. Ito, J. Nakahara, and R. Onaka, Magneto-optical Study of the Exciton States in $CsPbCl_3$, J. Phys. Soc. Jpn. **47**, 1927 (1979).

[70] S. T. A. G. Melissen, F. Labat, P. Sautet, and T. L. Bahers, Electronic properties of $PbX_3CH_3NH_3$ (X = Cl, Br, I) compounds for photovoltaic and photocatalytic applications, Phys. Chem. Chem. Phys. **17**, 2199 (2014).

[71] Since the kinetic energy terms in the Haken model contain the renormalized polaron masses (20), their curves in Fig. 10 are cut off before the strong coupling regime.

[72] R. W. Hellwarth and I. Biaggio, Mobility of an electron in a multimode polar lattice, Phys. Rev. B **60**, 299 (1999).

[73] C. Carabatos-Nédelec, M. Oussaïd, and K. Nitsch, Raman scattering investigation of cesium plumbochloride, $CsPbCl_3$, phase transitions, J. Raman Spectrosc. **34**, 388 (2003).

[74] A. Mahata, D. Meggiolaro, and F. D. Angelis, From large to small polarons in lead, tin, and mixed lead-tin halide perovskites, J. Phys. Chem. Lett. **10**, 1790 (2019).

[75] J. Tilchin, D. N. Dirin, G. I. Maikov, A. Sashchiuk, M. V. Kovalenko, and E. Lifshitz, Hydrogen-like wannier-mott excitons in single crystal of methylammonium lead bromide perovskite, ACS Nano **10**, 6363 (2016).

[76] V. S. Chirvony, S. González-Carrero, I. Suárez, R. E. Galian, M. Sessolo, H. J. Bolink, J. P. Martínez-Pastor, and J. Pérez-Prieto, Delayed luminescence in lead halide perovskite nanocrystals, J. Phys. Chem. C **121**, 13381 (2017).

[77] K. Galkowski, A. Mitioglu, A. Miyata, P. Plochocka, O. Portugall, G. E. Eperon, J. T.-W. Wang, T. Stergiopoulos, S. D. Stranks, H. J. Snaith, and R. J. Nicholas, Determination of the exciton binding energy and effective masses for methylammonium and formamidinium lead tri-halide perovskite semiconductors, Energy Environ. Sci. **9**, 962 (2016).

[78] A. Miyata, A. Mitioglu, P. Plochocka, O. Portugall, J. T.-W. Wang, S. D. Stranks, H. J. Snaith, and R. J. Nicholas, Direct measurement of the exciton binding energy and effective masses for charge carriers in organic-inorganic tri-halide perovskites, Nat. Phys. **11**, 582 (2015).

[79] H. Büttner and J. Pollmann, Excitons in polar semiconductors, Physica B+C **117**, 278 (1983).

[80] Z. Yang, A. Surrente, K. Galkowski, A. Miyata, O. Portugall, R. J. Sutton, A. A. Haghighirad, H. J. Snaith, D. K. Maude, P. Plochocka, and R. J. Nicholas, Impact of the halide cage on the electronic properties of fully inorganic cesium lead halide perovskites, ACS Energy Lett. **2**, 1621 (2017).

[81] G. Kresse and J. Furthmüller, Efficiency of ab-initio total energy calculations for metals and semiconductors using a plane-wave basis set, Comput. Mater. Sci. **6**, 15 (1996).

[82] P. E. Blöchl, Projector augmented-wave method, Phys. Rev. B **50**, 17953 (1994).

[83] J. P. Perdew, A. Ruzsinszky, G. I. Csonka, O. A. Vydrov, G. E. Scuseria, L. A. Constantin, X. Zhou, and K. Burke, Restoring the Density-Gradient Expansion for Exchange in Solids and Surfaces, Phys. Rev. Lett. **100**, 136406 (2008).

[84] H. Monkhorst and J. Pack, Special points for Brillouin-zone integrations, Phys. Rev. B **13**, 5188 (1976).

[85] J. Heyd, G. E. Scuseria, and M. Ernzerhof, Hybrid functionals based on a screened coulomb potential, J. Chem. Phys. **118**, 8207 (2003).

[86] D. Broberg, B. Medasani, N. E. Zimmermann, G. Yu, A. Canning, M. Haranczyk, M. Asta, and G. Hautier, PyCDT: A Python toolkit for modeling point defects in semiconductors and insulators, Comput. Phys. Commun. **226**, 165 (2018).

[87] S. P. Ong, W. D. Richards, A. Jain, G. Hautier, M. Kocher, S. Cholia, D. Gunter, V. L. Chevrier, K. A. Persson, and G. Ceder, Python Materials Genomics (pymatgen): A robust, open-source PYTHON library for materials analysis, Comput. Mater. Sci. **68**, 314 (2013).

[88] L. D. Whalley, Effmass: An effective mass package, J. Open Source Software **3**, 797 (2018).

[89] A. Togo and I. Tanaka, First principles phonon calculations in materials science, Scr. Mater. **108**, 1 (2015).

[90] K. Momma and F. Izumi, VESTA 3 for three-dimensional visualization of crystal, volumetric and morphology data, J. Appl. Crystallogr. **44**, 1272 (2011).

[91] J.-L. Calais and P.-O. Löwdin, A simple method of treating atomic integrals containing functions of r_{12}, J. Mol. Spectrosc. **8**, 203 (1962).

[92] Y. Suzuki and K. Varga, *Stochastic Variational Approach to Quantum-Mechanical Few-Body Problems* (Springer, Heidelberg, 1998).

[93] A. H. G. R. Kan and G. T. Timmer, Stochastic global optimization methods part I: Clustering methods, Math. Program. **39**, 27 (1987).

[94] A. H. G. R. Kan and G. T. Timmer, Stochastic global optimization methods part II: Multilevel methods, Math. Program. **39**, 57 (1987).

[95] M. J. D. Powell, *The BOBYQA Algorithm for Bound Constrained Optimization Without Derivatives*, Tech. Rep. NA2009/06 (Department of Applied Mathematics and Theoretical Physics, University of Cambridge, Cambridge, 2009).

[96] S. G. Johnson, The NLopt nonlinear-optimization package, http://github.com/stevengj/nlopt (unpublished).